NASA-CR-204810

SPECTRA OF HIGH-IONIZATION SEYFERT 1 GALAXIES: IMPLICATIONS FOR THE NARROW-LINE REGION

DAVID MOORE,[1] ROSS D. COHEN,[1] AND GEOFFREY W. MARCY[2]

ABSTRACT

We present line profiles and profile parameters for the narrow-line regions (NLRs) of six Seyfert 1 galaxies with high-ionization lines: MCG 8-11-11, Mrk 79, Mrk 704, Mrk 841, NGC 4151, and NGC 5548. The sample was chosen primarily with the goal of obtaining high-quality [Fe VII] $\lambda 6087$ and, when possible, [Fe X] $\lambda 6374$ profiles to determine if these lines are more likely formed in a physically distinct "coronal line region" or are formed throughout the NLR along with lines of lower critical density (n_{cr}) and/or ionization potential (IP).

We discuss correlations of velocity shift and width with n_{cr} and IP. In some objects, lines of high IP and/or n_{cr} are systematically broader than those of low IP/n_{cr}. Of particular interest, however, are objects that show no correlations of line width with either IP or n_{cr}. In these objects, lines of high and low IP/n_{cr} are remarkably similar, which is difficult to reconcile with the classical picture of the NLR, in which lines of high and low IP/n_{cr} are formed in physically distinct regions. We argue for similar spatial extents for the flux in lines with similar profiles.

Here, as well as in a modeling-oriented companion paper (Paper II), we develop further an idea suggested by Moore & Cohen that objects that do and do not show line width correlations with IP/n_{cr} can both be explained in terms of a single NLR model with only a small difference in the cloud column density distinguishing the two types of object. Overall, our objects do not show correlations between the full width at half-maximum (FWHM) and IP and/or n_{cr}. The width must be defined by a parameter that is sensitive to extended profile wings in order for the correlations to result. In Paper II, we present models in which FWHM correlations with IP and/or n_{cr} result only after simulating the lower spectral resolution used in previous observational studies. The models that simulate the higher spectral resolution of our observational study produce line width correlations only if the width is defined by a parameter that is more sensitive to extended profile wings than is the FWHM. Our sample of six objects is in effect augmented by incorporating the larger sample (16 objects) of Veilleux into some of our discussion.

This paper focuses on new interpretations of NLR emission-line spectra and line profiles that stem directly from the observations. Paper II focuses on modeling and complements this paper by illustrating explicitly the effects that spatial variations in electron density, ionization parameter, and column density have on model profiles. By comparing model profiles with the observed profiles presented here, as well as with those presented by Veilleux, Paper II yields insight into how the electron density, ionization parameter, and column density likely vary throughout the NLR.

Subject headings: galaxies: nuclei — galaxies: Seyfert — line: profiles

1. INTRODUCTION

One well-known observational feature of the narrow-line region (NLR) in Seyfert galaxies is the preponderance of blueward asymmetries in the emission-line profiles (e.g., Heckman et al. 1981; Whittle 1985a; Dahari & De Robertis 1988; De Robertis and Shaw 1990; Veilleux 1991a). To account for the asymmetry, it is accepted in general that the NLR velocity field is mostly radial and that some source of opacity, most likely dust, is present. However, a consensus regarding the direction of cloud flow has yet to emerge because the blueward asymmetry can be explained qualitatively by either internal obscuration in the case of inflow or by external obscuration in the case of outflow (e.g., Capriotti, Foltz, & Byard 1981).

Another well-known observational feature of the NLR is that the full width at half-maximum (FWHM) of emission lines often correlate with ionization potential (IP) and critical density (n_{cr}). This feature has been commonly used to argue for a velocity field increasing radially inward under the assumption that lines of low IP/n_{cr} are emitted less efficiently (for fixed emitting mass) close to the central source than lines of high IP/n_{cr} (e.g., Osterbrock 1981; De Robertis & Osterbrock 1984, 1986, Whittle 1985b; Appenzeller & Östreicher 1988; De Robertis & Shaw 1990; Veilleux 1991b).

By comparing the FWHM of [O I] $\lambda 6300$ to that of [S II] $\lambda 6716$ in Seyfert galaxies, and by comparing the FWHM of [O III] $\lambda 4363$ to that of [O III] $\lambda 5007$ in Seyfert 2 galaxies (in which there is little or no contamination from broad Hγ and/or Fe II emission), we have argued that the correlations are best interpreted as fundamentally with ionization potential rather than with critical density (Moore & Cohen 1994, hereafter MC). We also proposed a new interpretation that these correlations are a column density effect, in which case the correlations are also consistent both with constant ionization parameter and with velocity increasing outward. As we pointed out in MC, line width is correlated with neither critical density nor ionization potential in some objects. In these objects, the similarity between profiles spanning a broad range of ionization potential and critical density is inconsistent with a scenario in which lines of low and high IP/n_{cr} are formed in physically distinct regions. The [Fe VII]

[1] Center for Astrophysics and Space Sciences 0111, 9500 Gilman Drive, University of California, San Diego, La Jolla, CA 92093-0111.

[2] Department of Astronomy, University of California, Berkeley, Berkeley, CA 94720.

$\lambda 6087$ and [Fe x] $\lambda 6374$ lines, which are very sensitive to ionization parameter (MC), are particularly important in this regard, and we emphasize these lines here.

In § 3, we present a sample of narrow-line profiles in intermediate Seyfert galaxies. The sample was chosen with the goal of obtaining high-quality [Fe vii] $\lambda 6087$ and, when possible, [Fe x] $\lambda 6374$ profiles. The sample consists of MCG 8-11-11, Mrk 79, Mrk 704, Mrk 841, NGC 4151, and NGC 5548.

We discuss briefly details of the observations and of the data reduction and profile extraction in § 2. In § 3, we discuss general implications for the NLR of line profile features. This discussion is based on previous observational studies as well as on our own. It will be useful to have already highlighted those general features of NLR spectra that discriminate best between different NLR models when we discuss our spectra and profiles. In § 4 we discuss specific implications of our data for NLR models. This discussion is facilitated by references to models presented in a companion paper (Moore & Cohen 1996, hereafter Paper II). The most constraining feature of the observed line profiles is the similarity in some objects of the profiles of lines corresponding to a wide range of IP/n_{cr}, and with very different sensitivities to ionization parameter. In § 5, we confirm for our sample the well-known correlations of velocity shift and width with IP and n_{cr}. However, our sample, which includes one contradictory object (NGC 5548), is too small to confirm by itself the conclusion of MC that the correlations are fundamentally with ionization potential rather than with critical density. Finally, we summarize our results in § 6.

2. DATA ANALYSIS

2.1. *Observations and Reductions*

Observations were made with the 200 inch (5.08 m) Hale telescope and double spectrograph (Oke & Gunn 1982) on six nights in 1983 and on a seventh night in 1984. The double spectrograph incorporates a dichroic beam splitter to cover approximately 3100–5200 Å on the blue side and 5200–11000 Å on the red side. The blue side had an RCA 320 × 512 CCD with 30 μm pixels, which corresponds to a spatial scale of 0″8 pixel^{-1}. One DN (count) corresponds to 6 photoelectrons, and the readout noise was 8 DN pixel^{-1}. A 1200 g mm^{-1} grating blazed at 4700 Å yields a dispersion of 1.09 Å pixel^{-1} at 3500 Å (200 km s^{-1} FWHM). The red side had a TI 800 × 800 CD with 15 μm pixels, which corresponds to a spatial scale of 0″6 pixel^{-1}. One DN corresponds to 2 photoelectrons, and the readout noise was 5 DN pixel^{-1}. A 1200 g mm^{-1} grating blazed at 7100 Å yields a dispersion of 0.82 Å pixel^{-1} at 6300 Å (75 km s^{-1} FWHM).

Because of the small wavelength coverage, most observations required unique wavelength settings. Grating tilts were set by hand with a vernier reading, which could not be reset to a specified wavelength with high precision. For most observations, wavelength calibration lamps and flat-field exposures were taken immediately before or after the observation at the hour angle and declination of the start or end of the observation, in order to minimize errors due to flexure in the spectrograph. Occasionally, calibration exposures were taken between two identical setups on an object. All observations were made with a 1″ slit except one ($\lambda 4363$ in NGC 5548).

For all the data reduction, we used the astronomical data reduction software package VISTA, developed at Lick Observatory. Straightforward procedures were used for baseline and LED preflash subtraction (for exposures in the blue) as well as for flat-fielding.

For each column, the spatial profile of the sky background was modeled by a fourth-order polynomial fit outside those rows bracketing the spatial profile of the object. The procedure includes automatic detection and rejection of cosmic-ray events as well as of hot and cold pixels in the sky background. From each column of the exposure, we subtracted the sky background model for that column.

The orientation of the CCD was skewed slightly with respect to the grating rulings, resulting in a shift in the centroid of the spatial profile of about 3 pixels over the length of the spectrum. The spectrum was extracted from a symmetric window, typically 6–8 pixels wide, centered on a parabolic fit to the centroid curve. The extraction included interpolation to allow for fractional pixels.

The size of the window used for spectral extractions was chosen to be roughly the apparent full width at zero-intensity of the spatial profile of the nuclear continuum. Observations were acquired under a range of atmospheric seeing conditions as follows. Spectra of MCG 8-11-11 were acquired under 3″–4″ seeing. Spectra of Mrk 79 were acquired under 1″5 seeing. Separate spectra of Mrk 704 were acquired under 1″, 1″5, 2″, and 4″–5″ seeing. Spectra of Mrk 841 were acquired under 1″5 and 3″ seeing. Separate spectra, covering the same wavelength region, of NGC 4151 were acquired under 1″5 (Fig. 5a), and 4″–5″ (Fig. 5b) seeing. Spectra of NGC 5548 were acquired under 1″5–2″ seeing. Even for NGC 4151, the nearest Seyfert galaxy in the sample, and for which separate spectra were acquired under the most extreme differences in seeing, spectra obtained under different seeing conditions showed very small, if any, systematic differences.

The extracted spectra were wavelength calibrated using polynomial fits to the measured centroids and known wavelengths of approximately 10 comparison lines in the blue and approximately 15 lines in the red. The order of the polynomial ranged between 2 and 4 and resulted in an rms residual of 0.02–0.06 Å. The absolute accuracy of the wavelength calibration can be inferred only from the night-sky lines in the spectrum. Offsets between the wavelength-calibrated object spectra and those of the night sky were of the order of 0.2 Å in scans with night-sky lines strong enough to permit a reliable comparison. The absolute accuracy could be better than 0.2 Å because this is roughly the precision with which the centroids of night-sky lines can be calculated. After extracting each spectrum and correcting for atmospheric extinction, the spectrum of a standard star was used to flux calibrate the object spectrum.

Occasionally an emission line of interest is close in wavelength to an atmospheric absorption feature. To correct for the feature, we used a transmission curve derived from a normalized standard star spectrum, in which the depth of the absorption was determined empirically by comparing the depths of the absorption troughs in the object and standard star (which were observed at slightly different air mass).

There were two profiles that were seriously corrupted by atmospheric absorption, those of [S ii] $\lambda 6731$ in MCG 8-11-11 and of [S ii] $\lambda 6716$ in Mrk 79 (both by B band). We have

excluded these profiles from formal presentation and analysis. However, profile parameters were calculated nonetheless, and after correcting for the absorption, the parameters calculated for $\lambda6716$ in MCG 8-11-11 were in reasonable agreement with those calculated for $\lambda6731$. Similarly, the parameters of $\lambda6731$ in Mrk 79 agreed with those of $\lambda6716$. In Mrk 704, the B-band feature ends just blueward of [S II] $\lambda6716$, and inspection of the standard star shows that the atmospheric absorption does not affect the emission line directly. Nevertheless, the absorption complicated selection of the blue wing of the $\lambda6716$ profile enough that, after subtracting off an estimated underlying red wing of Hα broad, we considered the profile unsuitable for further analysis. The atmospheric absorption feature at 6280 Å is just redward of the [Fe VII] $\lambda6087$ profile in Mrk 704, but again inspection of the standard star spectrum shows that the line profile is not affected directly. The [Fe VII] line of Mrk 704 was not excluded from further analysis because the strength and shape of the adjacent continuum permitted reliable subtraction, despite the absorption feature. The [Ne III] $\lambda3869$ profile in MCG 8-11-11 is just blueward of Ca II absorption at 3935 Å from the Galaxy, but the absorption feature is narrow, and again neither the profile nor the continuum subtraction are affected seriously.

Several of the emission lines were observed in more than one scan either because several observations were made with the same grating tilt or because spectra overlapped enough in wavelength to include a common emission line. Such scans were averaged weighting by $(S/N)^2$, where the signal-to-noise ratio (S/N) in each spectrum was determined empirically from the rms scatter about a low-order polynomial fit to a featureless part of the continuum.

2.2. Profile Extraction

We chose the limits of each emission line by visual inspection and subtracted a polynomial fit to a featureless part of the adjacent continuum. The profiles were then placed on a velocity scale. Small heliocentric corrections were applied to the velocities as appropriate. In the ideal case, the zero point of the velocity scale corresponds to the recessional velocity of the NLR center of mass. The least subjective estimate of the NLR center-of-mass velocity is that of 21 cm radiation. We used a 21 cm measurement, taken from Heckman, Balick, & Sullivan (1978), for Mrk 79, NGC 4151, and NGC 5548. A 21 cm measurement was not available for the remaining objects. We used the peak of [O III] $\lambda5007$ for Mrk 704, the centroid of [O I] $\lambda6300$ for MCG 8-11-11, and the peak of [O I] $\lambda6300$ for Mrk 841. The appropriate measurement was picked from observational considerations such as the S/N, profile asymmetry, and/or the degree to which a profile peak could be determined unambiguously, rather than from model-dependent considerations in which a particular measurement is assumed a priori to best represent the galactic systemic velocity.

In some cases, the spread in cloud velocity is large enough to blend together the individual profiles of two nearby emission lines. To reconstruct the individual profiles, we used a deblending program developed at UCSD by Steve Bradley. The program allows a template profile to be defined from the data, from which model profiles can be derived by rescaling the template in intensity and by using interpolated profile fluxes to vary the wavelength and width of the template.

Further details of the appropriate deblending procedure

depend on the nature of the blend. We describe the deblending of four particularly important lines, [O III] $\lambda4363$ (high-density diagnostic) from broad and narrow Hγ, [Fe X] $\lambda6374$ (high-ionization parameter diagnostic) from [O I] $\lambda6363$, [O I] $\lambda6300$ (large column density diagnostic) from [S III] $\lambda6312$, and [S II] $\lambda\lambda6716$, 6731 (low-density diagnostic).

To subtract Hγ from [O III] $\lambda4363$, we used the broad and narrow components of Hβ to model the respective components of Hγ, scaling them in intensity and width and varying the position until the final profile matched, in a least-squares sense, that portion of the Hγ profile not contaminated by [O III] $\lambda4363$ emission. We did not assume that the ratios of the narrow and broad components are the same for both Hγ and Hβ. For Mrk 79 and NGC 5548, an analogous procedure was used to deblend [S III] $\lambda6312$ from [O I] $\lambda6300$ using [O III] $\lambda5007$ as a template [O I] profile. The net result here is to replace that portion of the [O I] profile contaminated by [S III] emission by a template [O III] $\lambda5007$ profile, where the template is fitted in intensity and width to match that portion of the [O I] profile not contaminated by [S III] emission. (The [O I] and [O III] profiles are similar to each other in Mrk 79 and NGC 5548.) To deblend [S III] from [O I] in NGCC 4151, we shifted and scaled the [O I] + [S III] blend itself to model the [S III] profile and subtracted the result from the [O I] + [S III] blend. To subtract [O I] $\lambda6363$ from [Fe X] $\lambda6374$, we used the profile of [O I] $\lambda6300$ scaled by 0.33, where the scale factor is derived from atomic parameters. To deblend [S II] $\lambda\lambda6716$, 6731, we used an iterative procedure with the blended $\lambda6731$ profile as an initial template. We fitted the blended $\lambda6731$ profile to that of the blended $\lambda6716$ profile with an intensity scale factor as the single free parameter. The resulting profile is a model of a deblended $\lambda6716$ profile. The model is poorly determined because the template $\lambda6731$ profile is highly contaminated by $\lambda6716$ emission. Nevertheless, the model $\lambda6716$ profile is subtracted from the blend at $\lambda6716$, resulting in a partially deblended $\lambda6731$ profile. The procedure is then repeated using the partially deblended $\lambda6731$ profile as a template. The result is a better model of a deblended $\lambda6716$ profile than that of the previous iteration because the $\lambda6731$ template is less contaminated by $\lambda6716$ emission. More than three iterations only degraded the S/N with little or no improvement in the deblending.

We did not apply a formal deblending procedure to reconstruct profiles of [N II] $\lambda6548$, Hα (narrow component), and [N II] $\lambda6584$. The only objects for which we attempted to analyze these profiles were those in which the narrow components were not blended with each other and the underlying component of broad Hα could be discerned by visual inspection and subtracted off in much the same way we subtracted off the continuum in other lines. The Hβ profile was used merely as a guide for the "continuum placement."

An atlas of the line profiles extracted from the reduced spectra is given in Figures 1-6. All the profiles presented here are normalized to the peak. Lower resolution studies, in which a large spectral range was obtained on a single night, resulted in more reliable relative flux estimates than did our own study. We include these relative flux estimates in Table 1. The dereddened emission-line fluxes for MCG 8-11-11, Mrk 79, Mrk 704, Mrk 841, and NGC 5548 are from Cohen (1983), and those (not corrected for reddening)

TABLE 1

NARROW EMISSION-LINE FLUX RELATIVE TO Hβ

Line	MCG 8-11-11	Mrk 79	Mrk 704	Mrk 841	NGC 4151	NGC 5548
[O II] $\lambda3727$........	3.24	2.20	0.66	0.99	1.47	1.33
[Fe VII] $\lambda3760$......	0.21	0.25	1.06	0.47	0.14	0.52
[Ne III] $\lambda3869$......	1.46	1.57	1.25	1.62	1.35	1.88
[O III] $\lambda4363$.......	0.32	0.48	0.53	0.18	0.34	1.23
He II $\lambda4686$.........	0.16	0.25	0.43	0.32	0.15	0.26
H I $\lambda4861$...........	1.00	1.00	1.00	1.00	1.00	1.00
[O III] $\lambda5007$.......	8.46	10.11	6.45	11.08	15.29	9.61
[Fe VII] $\lambda5721$......	0.08	0.17	0.52	0.07	0.11	0.10
He I $\lambda5876$..........	0.10	0.13	0.11	0.17	0.15	0.07
[Fe VII] $\lambda6087$......	0.10	0.28	0.74	0.30	0.22	0.35
[O I] $\lambda6300$.........	0.40	0.36	0.16	0.32	1.06	0.26
[S III] $\lambda6312$........	...	0.05	0.12	0.04	0.03	0.03
[Fe X] $\lambda6374$.......	0.06	0.11	0.49	0.11	0.12	0.08
H I $\lambda6563$...........	2.08	2.93	2.62	2.87	5.29	2.43
[N II] $\lambda6584$........	2.06	2.16	0.91	1.08	2.24	1.10
[S II] $\lambda6716$.........	0.58	0.72	0.22	0.35	0.82	0.21
[S II] $\lambda6731$.........	...	0.72	0.31	0.37	1.00	0.20

for NGC 4151 are from Boksenberg et al. (1975). The [Fe X] $\lambda6374$ line strength in NGC 4151 was determined from the $\lambda6374$ to $\lambda6300$ line strength ratio of Veilleux (1988) and the $\lambda6300$ line strength of Boksenberg et al. (1975), as $\lambda6374$ was not included in the latter study. These line strengths have implications for some of the models discussed in Paper II. For possible future reference, we have also included [S III] $\lambda6312$ relative line strengths based on our measured [S III] $\lambda6312$ to [O I] $\lambda6300$ line strength ratios and the previously published [O I] line strengths.

3. GENERAL IMPLICATIONS FOR THE NLR

Before discussing interpretations of the line profiles, we summarize some important characteristics of NLR model profiles that should not be overlooked. The basic goal is to provide interpretations that stem directly from the observed profiles to the extent possible, with only minimal reference to specific models. The most important premise is that the preponderance of blueward asymmetry constrains the highest velocity clouds to move mostly in the radial direction and precludes the presence of a broad distribution of velocities at each radial coordinate, r (asymmetric distributions of gas would produce red and blue asymmetries with equal likelihood). Neglecting obscuration, a spherical shell of delta function–emitting clouds moving radially with velocity v_0 yields a boxcar profile with half-width v_0. As can be inferred directly by visual inspection, replicating the observed profiles requires that either boxcar profiles with a range of velocity width must be superposed, or else assumptions such as purely radial cloud flow or a spherical NLR must be relaxed.

In MC we showed that the profile wings are not sensitive to either the orientation or the opening angle of a biconical line-emitting structure (with the caveat that the velocity field is renormalized appropriately when the line of sight falls outside the biconical structure), even though the profile core is. In Moore (1994, 1995), it is demonstrated that the blue wing is not very sensitive to details of the obscuration, whether internal or external to the emitting clouds. Thus, it is possible to interpret the blue wings readily in the context of a simplified model NLR even though collimated emission and obscuration are likely present. This point is worth emphasizing because it follows then from the absence of a broad distribution of cloud velocities at each r (see above)

that the range in height and in velocity width of boxcar profiles that must be superposed to replicate the observed blue wings relates directly to the spatial dependence of the line emission. For lines that are useful diagnostics of electron density (n_e), column density (N_{col}), and/or ionization parameter (Γ), the spatial dependence of the line emission in turn corresponds directly to how n_e, N_{col}, and Γ vary spatially throughout the NLR. The effects of spatial variations in n_e, N_{col}, and Γ are discussed qualitatively when we discuss the profiles of individual objects. The effects are illustrated more explicitly (though less independent of detailed modeling) in Paper II.

It is an observational fact that, in some objects, line profiles of high and low IP have very similar blue wings (see the discussion in MC as well as the profiles presented in § 3 and in Veilleux 1991a). It follows that if the velocity field is at all close to monotonic, then there is emission into lines of both high and low IP at each r, which could arise in either of two scenarios.

The first possible scenario is that individual clouds are stratified in ionization. The second possible scenario is that there is a broad distribution in the electron density of unstratified clouds and, therefore, in Γ at each r. Throughout this paper, we use the term "stratified cloud" to denote a single cloud of sufficient ionization stratification to emit [Fe X] and/or [Fe VII] lines from the front as well as [O I] and [S II] lines from the back. An "unstratified cloud" is optically thin to the photoionizing continuum so that a single ionization state describes the entire cloud. It is worth pointing out that blueward asymmetry and stratified clouds are consistent with either inflow or outflow according to whether the obscuration is mostly internal or external, respectively. Because the applicability of the first scenario is fundamental to our detailed modeling (Paper II) and to several of our conclusions, we outline here why we believe the first scenario applies. We note, however, that work favoring the second scenario is underway (Komossa & Schulz 1994; Tsvetanov et al. 1994). Our arguments for stratified clouds are as follows:

1. Clouds of very different n_e, but at the same r, cannot all be pressure confined. Because the equilibrium temperature of photoionized gas varies only slightly with n_e (MC), there is a narrow range of n_e at each r that can be in pressure equilibrium either with the intercloud medium

(ICM) or with a magnetic field. Because the cloud expansion timescale is a small fraction of the crossing time, a broad distribution of n_e at each r would require that clouds are continually created and destroyed (this has been suggested for broad-line region [BLR] clouds based on a stability analysis [Krinsky & Puetter 1992]).

2. A contrived distribution of n_e must be invoked for the second scenario so that each n_e contributes comparable flux to the appropriate emission line. Considering that the volume emissivity for optically thin gas is $j \propto n_e^2$, and the emission per fixed mass is proportional to n_e, arranging for clouds differing by several decades in n_e to produce comparable emission-line flux at each r, as observations require, is not trivial.

3. An inflow model requires stratified clouds to explain the preponderance of blueward asymmetry. An outflow model (with external obscuration) can accommodate unstratified clouds, but a mechanism must be found to outwardly accelerate clouds of very different density to nearly the same velocity. Otherwise, a broad distribution of projected velocity at each r, and consequently symmetric profiles, would result. In principal, clouds of very different n_e can be accelerated to similar velocities over very different length scales. This scenario could produce distinct coexisting velocity fields, with different lines coming from different underlying cloud populations at different r. However, to account for the striking similarity in the profiles of different lines in some objects, this exceedingly contrived scenario requires that the variation of emission-line flux with projected velocity is virtually identical for lines in which the variation of flux with r is very different.

4. While lines of high and low IP/n_{cr} are very similar in some objects, the high IP/n_{cr} lines are systematically broader in other objects. Both types of objects would not be explained naturally by a broad distribution in n_e and Γ at each r. Actually, both types of objects are also not easily explained in the classical picture of the NLR in which the highest velocity clouds are at small r, where lines of low n_{cr} are collisionally suppressed, resulting in systematically narrower low n_{cr} lines. To explain both types of objects in the classical picture of the NLR, the two types of objects must differ in the maximum n_e by several decades, which is the relevant range of n_{cr}. In Paper II, we present models in which line width correlations are a natural consequence of outward acceleration and of $N_{col} \propto r^{-4/3}$, the latter resulting from spherical clouds of constant mass and with constant ionization parameter. In these models, objects in which the low-ionization potential lines are broad and narrow differ in N_{col} by factors of only order unity.

4. INDIVIDUAL OBJECTS

4.1. MCG 8-11-11

The profiles extracted from MCG 8-11-11 spectra are plotted in Figure 1. We used the [O I] $\lambda6300$ line rather than [O III] $\lambda5007$ to estimate the systemic velocity of this object because $\lambda6300$ is more symmetric than $\lambda5007$, and an asymmetric profile yields an underestimated systemic velocity due to obscuration effects. We used the centroid rather than the peak because the peak of [O I] $\lambda6300$ is fairly flat-topped, so the peak location is ambiguous.

The [O II] $\lambda3727$ profile is a composite of the doublet, $\lambda3726 + \lambda3729$, corresponding to a separation of 217 km s^{-1}. The blue wing of $\lambda3727$ arises mostly from $\lambda3726$ emis-

sion. Clearly, from the apparent extent of the blue wing in Figure 1a, there are clouds with $v \approx -1000$ km s^{-1} appreciably emitting $\lambda3726$. The critical density of this line is 3×10^3 cm^{-3}, so the electron density of the $v \approx -1000$ km s^{-1} clouds emitting $\lambda3726$ does not greatly exceed 10^4 cm^{-3}.

As is the case with the profiles of Veilleux (1991a), the presence of a substantial velocity gradient across the NLR can be inferred by visual inspection of the profiles. In particular, note that a similar range of radial velocity can be inferred for all the profiles shown in Figure 1 (i.e., for each of the profiles, a substantial range in velocity width of boxcar profiles must be superposed to replicate the blue wing). In the absence of a broad distribution of cloud velocity at each r (§ 3), the similar range of radial velocity corresponds to similar spatial extents for the line emission. In the case of [Fe VII] $\lambda6087$, the similar spatial extent suggests a roughly constant ionization parameter throughout the NLR because [Fe VII] $\lambda6087$ is much more sensitive to ionization parameter than the other lines (MC). In the case of [O I] $\lambda6300$, the similar spatial extent suggests that the clouds are also optically thick to the photoionizing continuum throughout the NLR. The same consideration could also suggest that the low-density limit ($n_e \ll n_{cr}$) is valid throughout the NLR for even the lowest critical density lines ([O II] $\lambda3727$ and [S II] $\lambda\lambda6716, 6731$) because the effects of collisional de-excitation are apparent in neither the wings nor in the cores of these lines. Although the effects of collisional de-excitation on the profiles are illustrated explicitly in the detailed kinematical models of Paper II, they can also be discerned qualitatively as follows. If the NLR is spherical, and if obscuration can be neglected, and if the velocity field is radial even for the lowest velocity clouds, then the line profile is a simple superposition of boxcar profiles. Collisional de-excitation effects in the highest velocity clouds would be evident if the low critical density line profiles were lacking a contribution from the highest velocity boxcar profiles (i.e., the profile wings). Collisional de-excitation effects in the lowest velocity clouds would be evidenced by a broad flat profile peak (there would be no contribution from the lowest velocity boxcar profiles). Absence of collisional de-excitation effects throughout the [O II] $\lambda3727$ and [S II] $\lambda\lambda6716, 6731$ profiles would then limit the cloud electron density to $n_e \lesssim 10^4$ cm^{-3} throughout the NLR. However, the NLR model we favor includes $n_e \approx 10^6$ cm^{-3} gas (see Paper II, MC, and Moore 1994) and requires emission from low-density and low-velocity gas outside the (parameter space of the) NLR model to account for the [O II] $\lambda3727$ and [S II] $\lambda\lambda6716, 6731$ profile cores.

4.2. Mrk 79

The profiles extracted from Mrk 79 spectra are plotted in Figure 2. We have presented the profile of [S II] $\lambda6731$ rather than that of [S II] $\lambda6716$ because the latter is badly corrupted by the B-band absorption feature. The [Fe X] $\lambda6374$ profile is of such poor quality that almost nothing can be said about the NLR based on this profile except that there are [Fe X] $\lambda6374$-emitting clouds with $v \approx -1000$ km s^{-1} and that there is some range of (radial) velocity sampled by the $\lambda6374$-emitting clouds because the profile is not a single boxcar profile. However, $\lambda6374$ is so sensitive to ionization parameter (MC) that even this small piece of information is useful and implies that the ionization parameter is roughly constant over whatever range of velocity can be
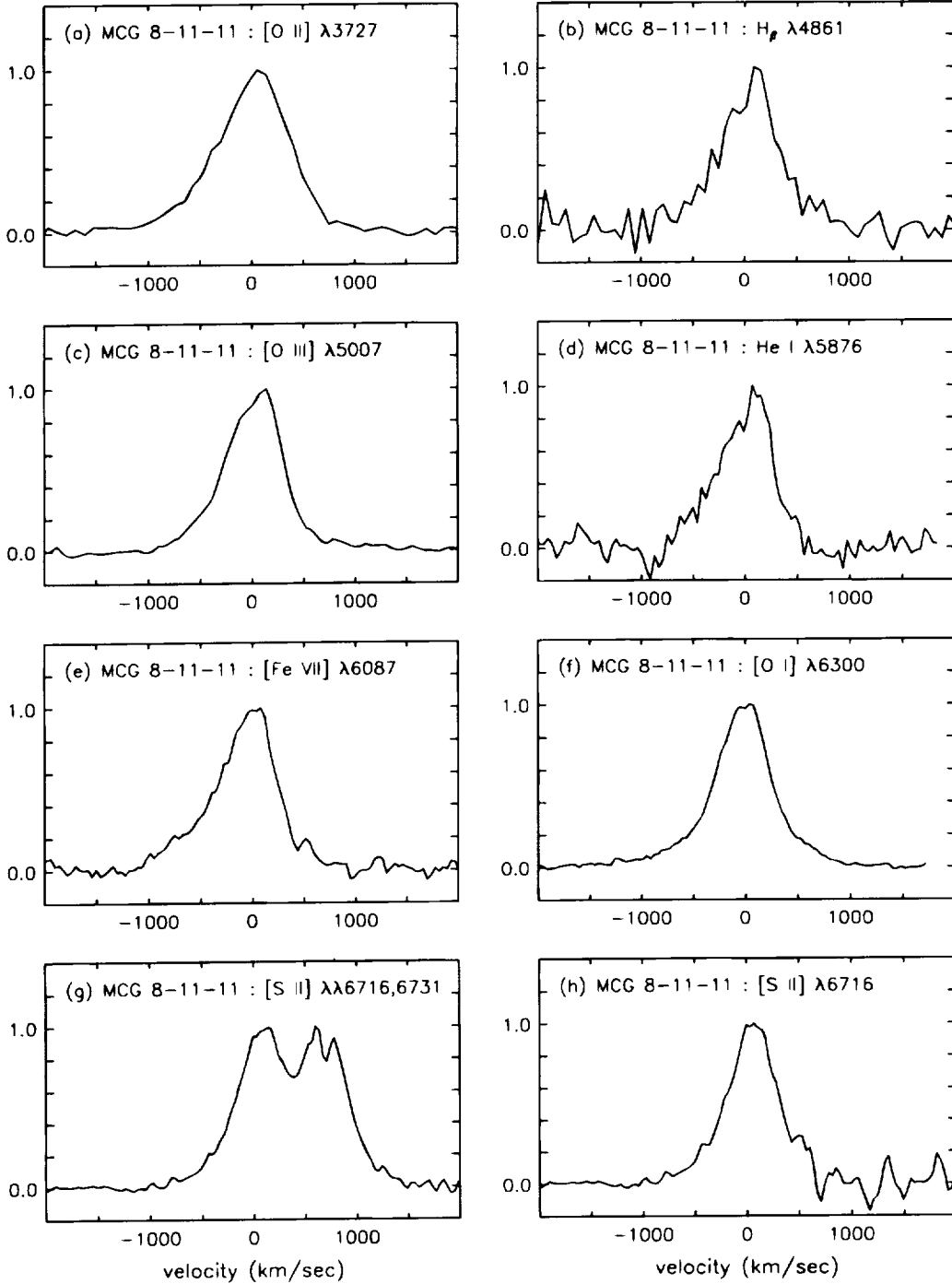
FIG. 1.—Narrow emission-line profiles extracted from spectra of MCG 8-11-11. A scenario in which the NLR can be decomposed into physically distinct regions in which the low-ionization potential/critical density lines and the high-ionization potential/critical density lines are formed is inconsistent with the similarity in the profiles shown here. To account for the similarity in the profiles requires significant emission in each line over a large fraction of the NLR. In particular, note the similar velocity ranges sampled by [S II] $\lambda6716$ and [O I] $\lambda6300$. These lines differ by three decades in critical density. Panels (g) and (h) represent [S II] before and after deblending, respectively. The trough of the B-band absorption feature coincides with the peak of $\lambda6731$. Due to the coincidence in wavelength, the B-band correction is poor, as evidenced by the residual feature at the peak of $\lambda6731$. Although $\lambda6731$ was excluded from further analysis, profile parameters were calculated, nonetheless, and they were in reasonable agreement with those of $\lambda6716$.

inferred from the profile. Note that the [Fe VII] $\lambda6087$ profile has an extended blue wing that is not present in other profiles (we exclude the [Fe X] $\lambda6374$ profile from the discussion owing to the very low S/N in the wings). The FWHM of [Fe VII] $\lambda6087$ is similar to that of [O III] $\lambda5007$, but a width parameter defined at a lower fraction of the peak intensity is significantly larger for [Fe VII] than for

[O III]. Our favored models ($n_e \propto r^{-2}$, $v \propto r^{1/2}$, and $N_{col} \propto r^{-4/3}$) show the same effect as well (Paper II).

In both objects, MCG 8-11-11 and Mrk 79, the [Fe VII] $\lambda6087$ profile is broad. The [O I] $\lambda6300$ profile is either broad (MCG 8-11-11) or narrow (Mrk 79). When [O I] is broad, [S II] is also broad, and when [O I] is narrow, [S II] is also narrow. This is consistent with the trend discussed
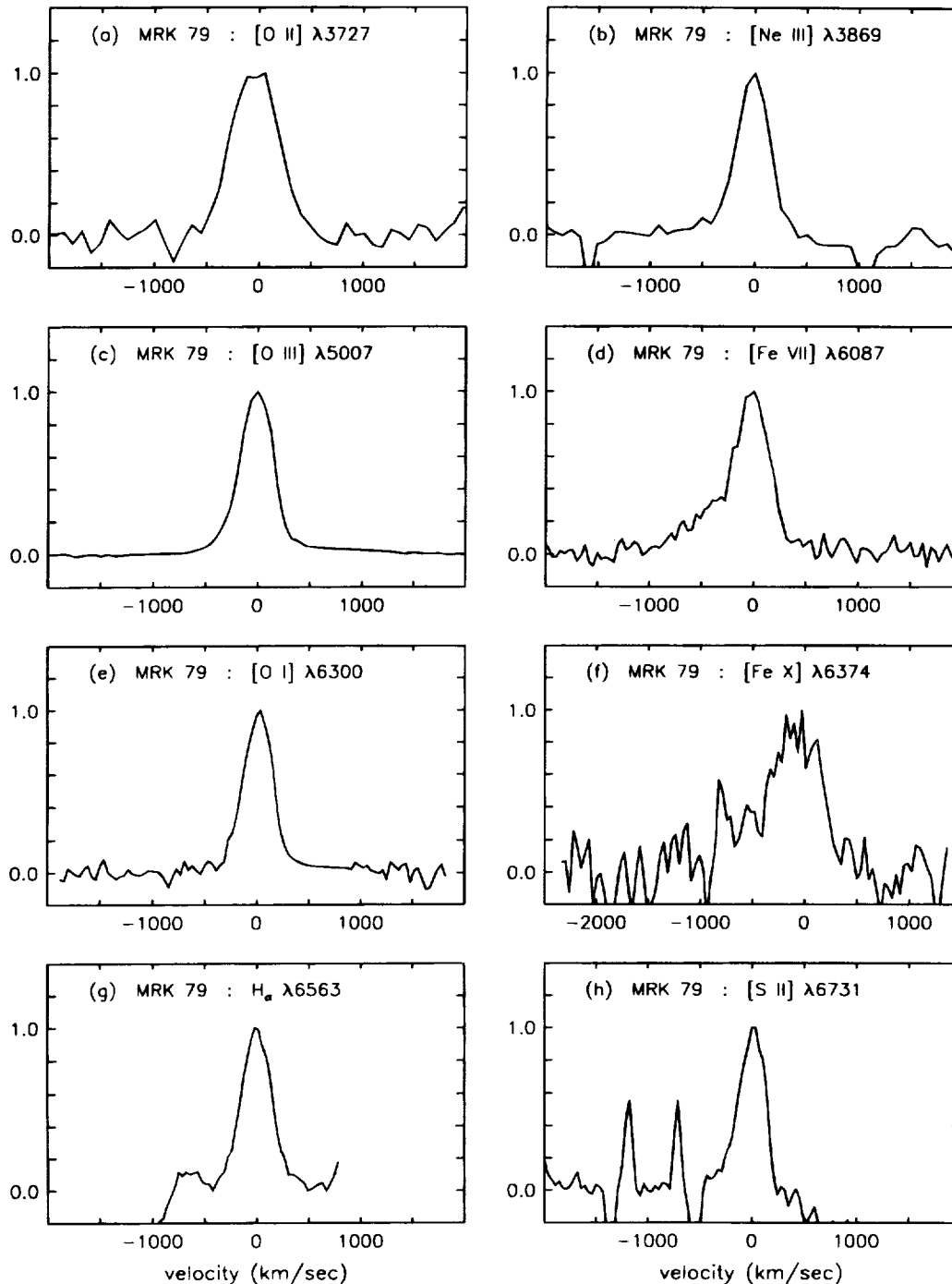
FIG. 2.—Narrow emission-line profiles extracted from spectra of Mrk 79. Note that in Mrk 79, unlike in MCG 8-11-11, [O I] and [S II] are both narow relative to [Fe VII]. We explain the difference between MCG 8-11-11 and Mrk 79 in terms of identical NLRs except that clouds at the inner radius of MCG 8-11-11 start out with somewhat higher column density than those of Mrk 79. In this scenario for Mrk 79, N_{col}/N_{min} decreases to less than one before the clouds reach their maximum velocity at the outer radius, while in the MCG 8-11-11 scenario, $N_{col}/N_{min} > 1$ throughout the NLR.

in MC for a much larger sample (≈ 50) of objects. The trend for [O I] and [S II] to have similar widths poses a difficulty for interpreting line width correlations as fundamentally with n_{cr} because these lines differ in n_{cr} by three decades.

We can explain the difference between MCG 8-11-11 and Mrk 79 in terms of identical NLRs, except that clouds at the innermost radius in MCG 8-11-11 start out with somewhat higher column density than those in Mrk 79. In Mrk 79, N_{col} decreases to less than N_{min} before the clouds reach their

maximum velocity at the outermost radius, while in MCG 8-11-11, $N_{col}/N_{min} > 1$ throughout the NLR. We define N_{min} as the minimum column density needed for an [O I] $\lambda6300$–emitting zone to exist in the back of the clouds. Referring to the models of Paper II, MCG 8-11-11 corresponds to model 3 and Mrk 79 corresponds to model 4. We postulate that our model for Mrk 79 is representative of objects that show correlations of line width with ionization potential, while our model for MCG 8-11-11 is representative of objects that do not.

4.3. Mrk 704

The profiles extracted from Mrk 704 spectra are plotted in Figure 3. The systemic velocity was estimated from the peak of [O III] $\lambda5007$. Note the extended blue wing in the [Fe VII] profile, from which it is clear that the [Fe VII]–emitting clouds sample a wide range of velocity. Of even greater significance, a substantial range of velocity can also be inferred from the [Fe X] $\lambda6374$ profile, which is extremely sensitive to ionization parameter (MC). Because of the wide range of cloud velocity that can be inferred directly from the observed [Fe X] $\lambda6374$ profile, our case for constant ioniza-

tion parameter is strongest for Mrk 704, NGC 4151, and NGC 5548.

As is the case for Mrk 79, the extended blue wing in the [Fe VII] profile of Mrk 704 is not evident in the profiles of [O I] $\lambda6300$ and [S II] $\lambda\lambda6716$, 6731. The obviously low quality of the [O I] and [S II] profiles precludes a more definitive statement, however. The [O I] and [S II] profiles of Mrk 79 are suggestive of the following interesting effect, which is evident in model 4 of Paper II though the effect is inconclusive here owing to the low quality of these profiles. The effect is that a width parameter defined in the wings is
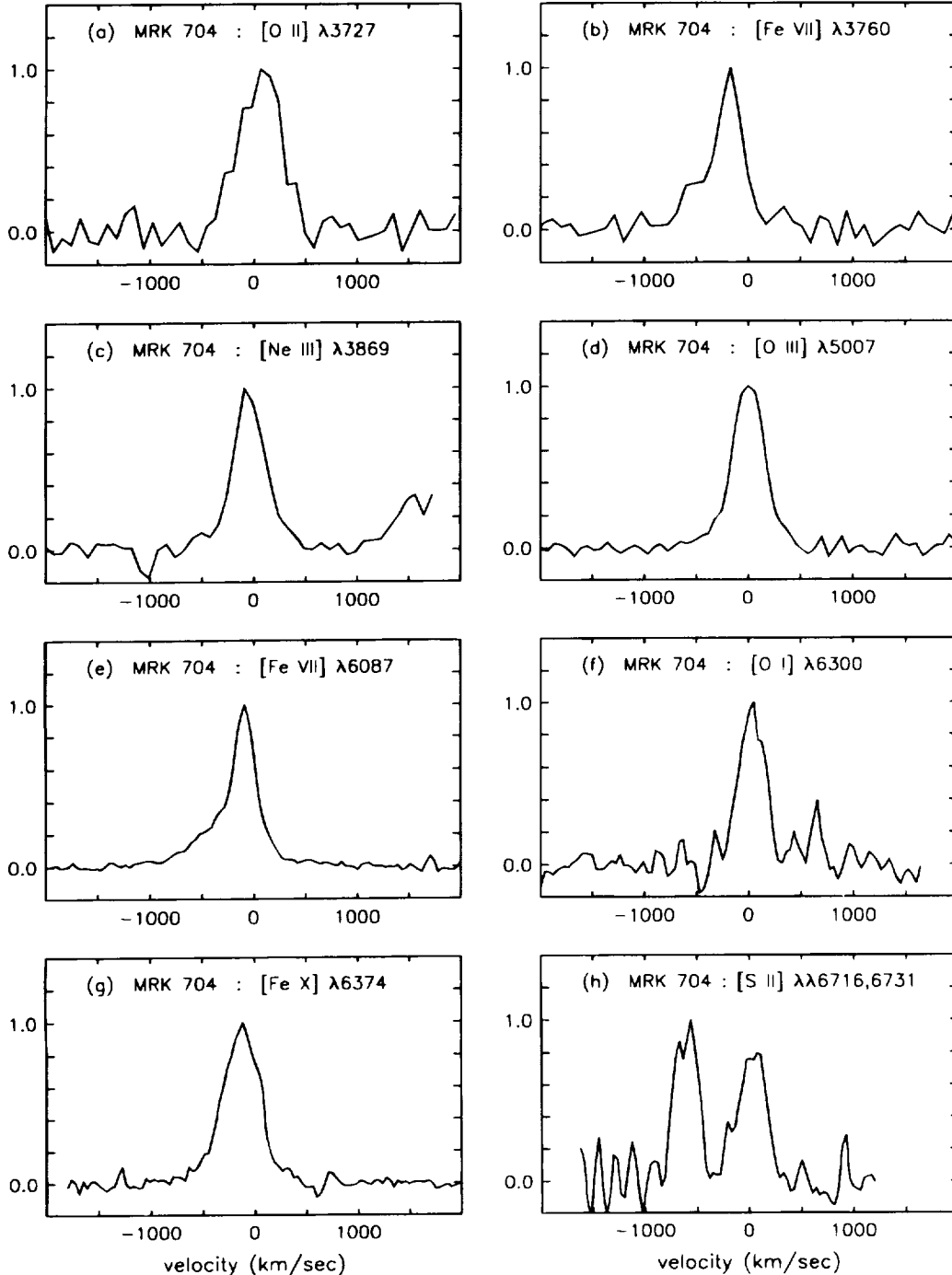

FIG. 3.—Narrow emission-line profiles extracted from spectra of Mrk 704. As is the case in Mrk 79, the extended blue wing of the [Fe VII] profile of Mrk 704 is not evident in the [O I] and [S II] profiles.

larger for [Fe VII] than for [O I] and [S II], even though the FWHM is about the same, and the width at any fraction of the peak intensity is similar for [O I] $\lambda6300$ and [S II] $\lambda6716$.

4.4. Mrk 841

The profiles extracted from Mrk 841 spectra are plotted in Figure 4. The systemic velocity was estimated from the peak of [O I] $\lambda6300$. Note the very extended ($\gtrsim 1000$ km s^{-1}) blue wing of the [Fe VII] $\lambda6087$ profile. This wing is not present in other profiles (the [Fe X] profile is inconclusive).

For Mrk 841, unlike Mrk 79 and Mrk 704, the width at any fraction of the peak intensity is greater, almost up to the peak itself, for [Fe VII] than for [O I] and [S II]. Note also that the [S II] profiles are narrow, and the [O I] profile is narrow as well, in keeping with the trend discussed here and in MC. Thus, we assert that Mrk 841 is best explained by model 4.

4.5. NGC 4151

The profiles extracted from NGC 4151 spectra are plotted in Figure 5. We include two profiles (Figs. 5a–5b) of
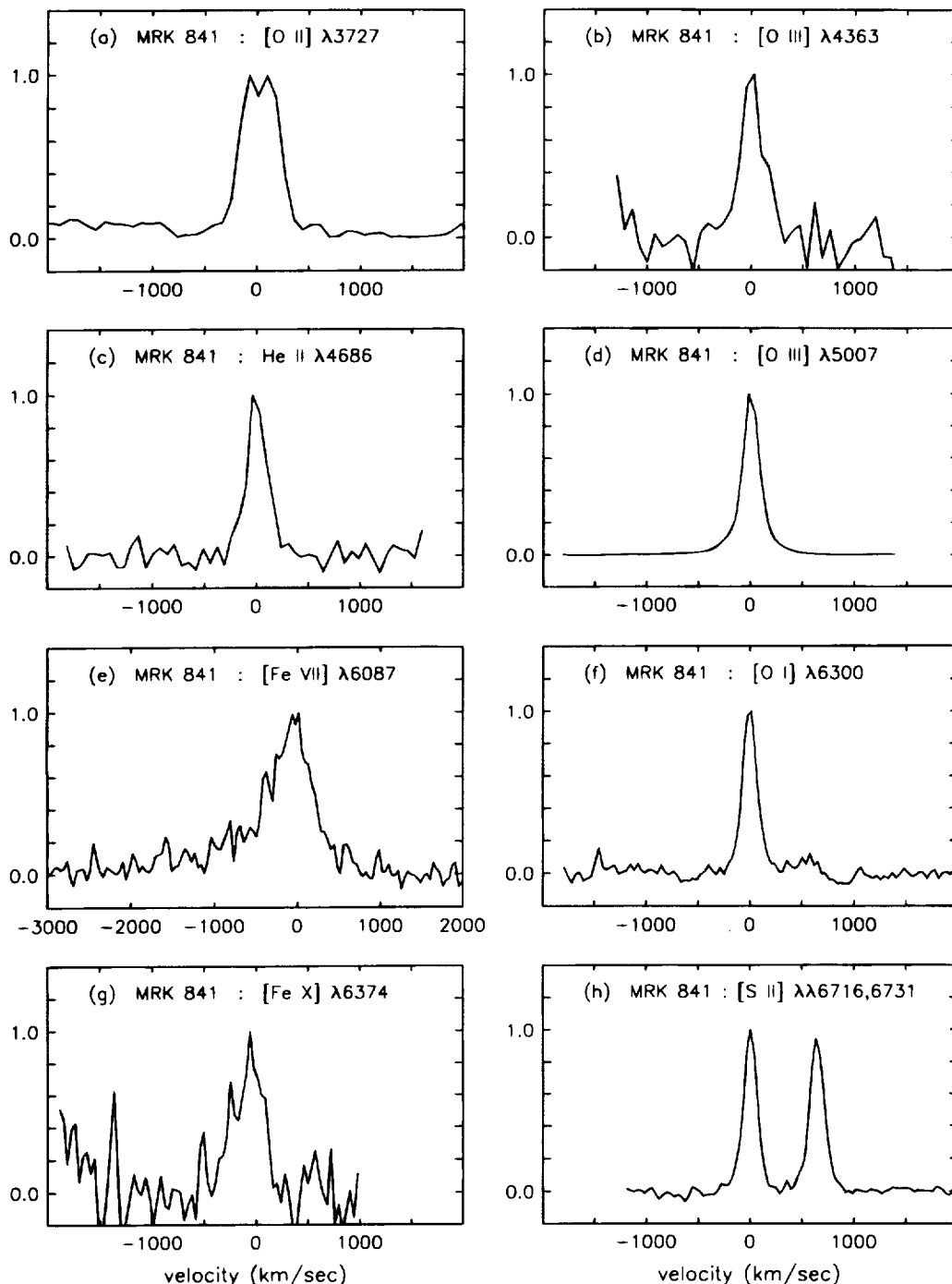

FIG. 4.—Narrow emission-line profiles extracted from spectra of Mrk 841. Note that [O I] and [S II] are both very narrow relative to [Fe VII]. This is in keeping with a general trend: when [O I] is narrow, [S II] is narrow as well, and when [O I] is broad, [S II] is broad also. These lines differ in critical density by three decades, however.
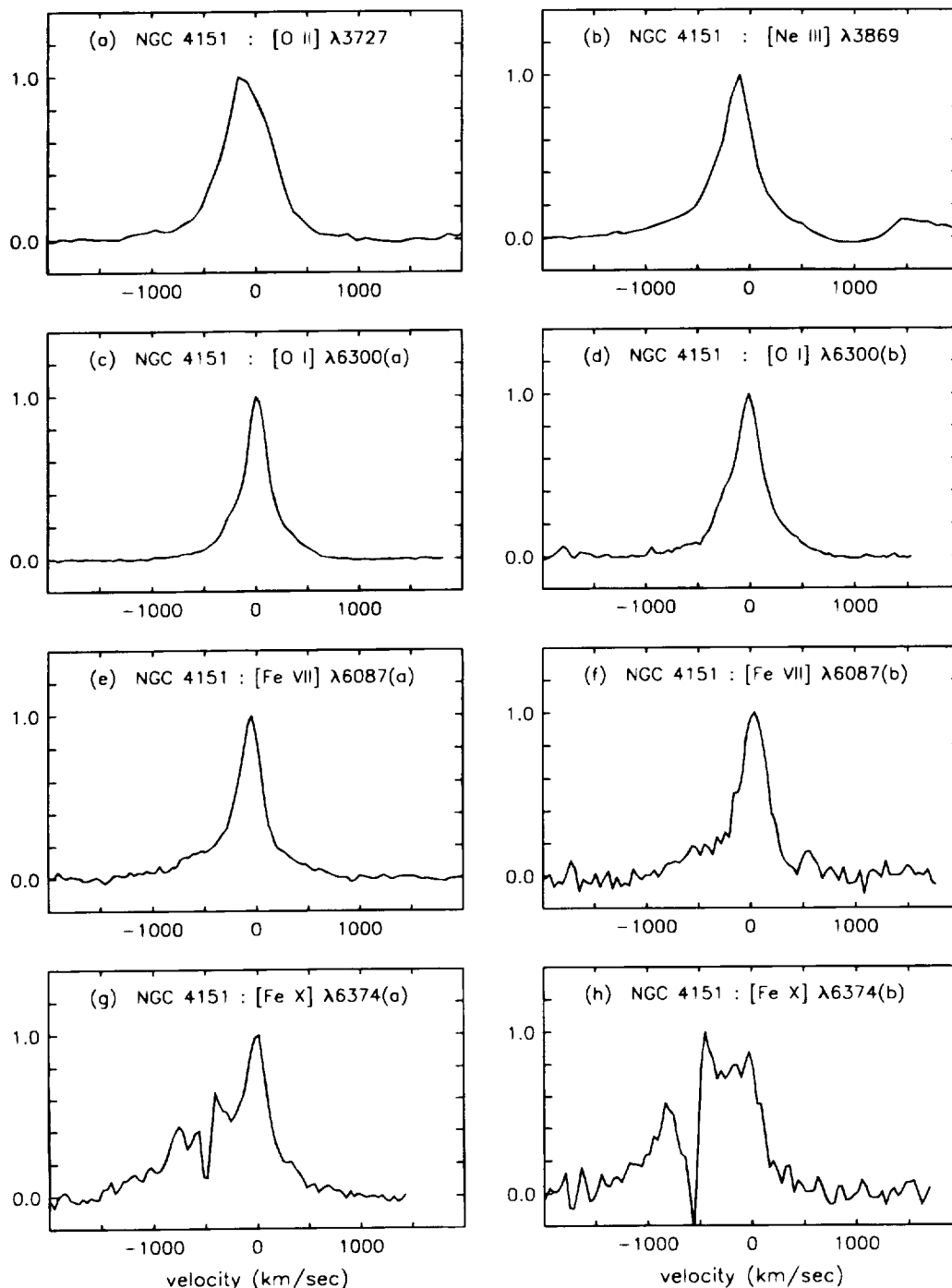
Fig. 5.—Narrow emission-line profiles extracted from spectra of NCG 4151. We include two profiles, (a) and (b), of [O I], [Fe VII], and [Fe X] corresponding to two observations 105 days apart because the Fe lines of NGC 4151 have been reported in the literature as possibly variable (Penston et al. 1984). Note that the [Fe VII] profiles of NGC 4151 and Mrk 704 are virtually identical, suggesting a very simple common acceleration mechanism. Note also that the [Fe X] profile has the same overall characteristics as the [Fe VII] profile of any object presented thus far. This would not likely result if [Fe X] and [Fe VII] were emitted in physically distinct regions.

[O I] $\lambda6300$, [Fe VII] $\lambda6087$, and [Fe X] $\lambda6374$ corresponding to two observations 105 days apart. NGC 4151 is highly variable in its continuum luminosity, and the forbidden Fe lines of NGC 4151 have been reported as possibly variable (Penston et al. 1984). We see no compelling evidence of variability in the profiles here (of course, our time baseline is much smaller than the 3 year baseline of Penston et al.).

As in every object presented thus far, the [Fe VII] profile of NGC 4151 shows a very extended ($\gtrsim 1000$ km s^{-1}) blue wing. The similarity in the [Fe VII] profiles of NGC 4151

(Fig. 5a) and of Mrk 704 is striking. The profiles are virtually identical. In all five objects whose profiles we have presented thus far, the [Fe VII] profiles are very similar and do not differ even in an overall scale factor in the velocity width. In every object, we can infer [Fe VII] emission out to $v \approx 1000$ km s^{-1} and not much higher. The remarkable similarity in the [Fe VII] profiles of each object suggests a very simple common acceleration mechanism. Likewise, Whittle (1991) has pointed out previously that the similarity in the [O III] $\lambda5007$ profiles from a large number of objects
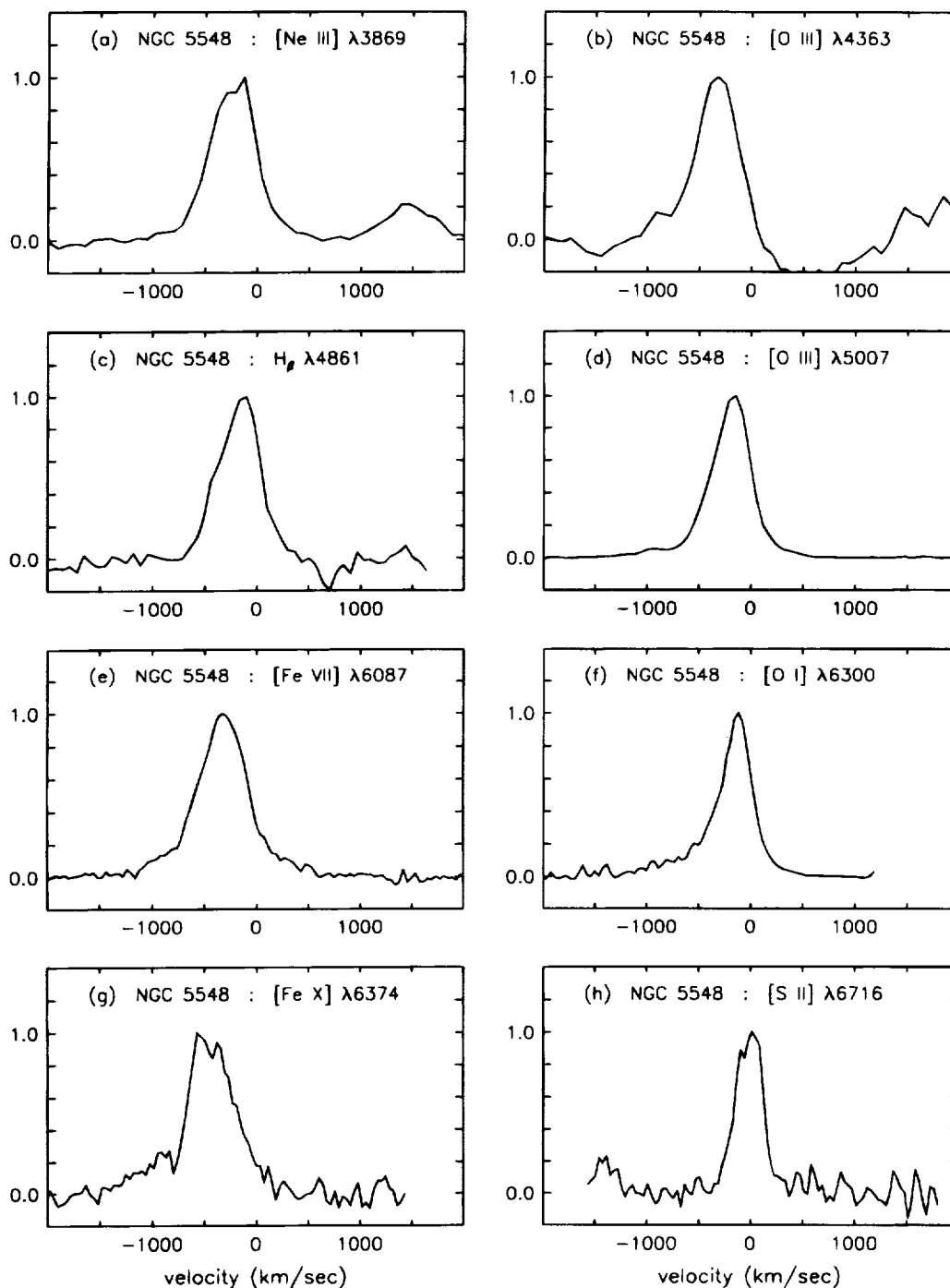
Fig. 6.—Narrow emission-line profiles extracted from spectra of NGC 5548. Note that the [O I] profile is broad, but the [S II] profile is narrow. This is in contrast to a general trend discussed here and in MC.

suggests a common acceleration mechanism for the $\lambda5007$-emitting gas.

The similarity in the [Fe VII] $\lambda6087$ profiles of NGC 4151 and Mrk 704 has possible implications concerning how representative our sample of Seyfert 1 galaxies is. Because the sample was chosen with the goal of obtaining high-quality [Fe VII] $\lambda6087$ and, when possible, [Fe X] $\lambda6374$ profiles, selection was biased toward objects with strong $\lambda6087$ and $\lambda6374$ emission. It is quite possible that the same properties of the same that allow us to obtain reliable $\lambda6087$ and $\lambda6374$ profiles also render the sample unrepresentative of Seyfert 1 galaxies in general. The forbidden Fe line strengths of NGC

4151 are more representative of a typical Seyfert 1 galaxy than those of Mrk 704. We were able to extract reliable $\lambda6087$ and $\lambda6374$ profiles of NGC 4151 because our spectra have high S/N due to this object's brightness. Of the six objects in our sample, the $\lambda6087$ line of Mrk 704 is the strongest relative to Hβ (0.87), while that of NGC 4151 is the weakest (0.07). The object in our sample with the strongest $\lambda6087$ line and an object that is representative in its $\lambda6087$ line strength of a typical Seyfert 1 galaxy have virtually identical profiles, which suggests that the density and velocity profiles throughout the NLR are very similar in both objects. That is, we do not infer any important differ-

ences between Mrk 704 and NGC 4151 other than the different [Fe VII] line strengths. The argument could be tested by selecting at random one or two objects with weak [Fe VII] line strengths and investing the telescope time required to obtain S/N comparable to that of our profiles of [Fe VII] $\lambda6087$ in both Mrk 704 and NGC 4151. We note also that, although Veilleux (1991a) did not include any [Fe X] $\lambda6374$ profiles and included [Fe VII] $\lambda6087$ profiles for only Mrk 359 and NGC 4151, the lower ionization line profiles in his sample are similar to those in our own sample.

Any of the [Fe VII] profiles presented thus far will suffice more or less as an archetypical [Fe VII] $\lambda6087$ profile. The [Fe X] $\lambda6374$ profile of NGC 4151 has the same overall characteristics as the [Fe VII] $\lambda6087$ profile of any object. This suggests that [Fe X] is emitted in a region that is similar spatially to the region of [Fe VII] emission rather than from a physically distinct region close to the central source with $n_e \approx n_{cr} = 5 \times 10^9$ cm^{-3}. Our case for constant-ionization parameter, based on the forbidden Fe lines, is probably strongest for NGC 4151. In Paper II we present some models in which ionization parameter decreases outward but not so much that the model [Fe VII] $\lambda6087$ profile is inconsistent with observations. The [Fe X] $\lambda6374$ profile, on the other hand, is extremely sensitive to ionization parameter. Almost any spatial variation at all in the ionization parameter results in a synthetic [Fe X] $\lambda6374$ profile that is, contrary to observations, different from that of [Fe VII] $\lambda6087$ and other profiles.

NGC 4151 is like MCG 8-11-11 in that the [Fe VII] and [O I] profiles are very similar. Thus, we infer similar spatial extents to the [O I] and [Fe VII] line emission, which requires that either [O I] and [Fe VII] are emitted from clouds at the same r but with very different n_e, or else the emitting clouds are individually stratified in ionization. We argued for the latter in § 3. We do not have a spectrum of NGC 4151 that includes the [S II] lines, but the blue wing of the [S II] $\lambda6716$ profile presented by Veilleux (1991a) is very similar to that of [O I] $\lambda6300$ (either ours or Veilleux's). Again, this agrees with the trend discussed here and in MC, namely, when [O I] is broad, [S II] is broad as well.

4.6. NGC 5548

The profiles extracted from NGC 5548 spectra are plotted in Figure 6. The overall characteristics of the [Fe VII] profile from NGC 5548 are consistent with the [Fe VII] profile from the above five objects, although we cannot infer as wide a range of cloud velocity from this profile. The latter could be due to a smaller v_{max}/v_{min} for the [Fe VII] $\lambda6087$-emitting gas in this object or perhaps to a larger chaotic component of the velocity field. We define v_{max} as the maximum radial velocity of NLR clouds. It is the velocity at the innermost or outermost NLR radius, according to whether the cloud velocity increases inward or outward. Similarly, v_{min} is the minimum radial velocity of NLR clouds. When the ratio of the maximum radial velocity in the NLR to the minimum radial velocity (v_{max}/v_{min}) is decreased, the wings are less pronounced, and the result is a profile closer to that of a boxcar function.

Note that our discussion of the [Fe X] profile of NGC 4151 applies to NGC 5548 as well. The blue wing of the [Fe X] profile extends out to about 1500 km s^{-1} relative to the systemic velocity (but about 1000 km s^{-1} relative to the peak). Even though v_{max}/v_{min} may not be as large for this

profile as other profiles presented thus far, a wide range of radial velocity is clearly present in this profile. Thus, the ionization parameter will be fairly constant over much of the NLR in NGC 5548. The blue wing of [O I] is about as extended as that of [Fe X] (i.e., significant flux out to a projected velocity of about -1000 km s^{-1}), from which we infer that the clouds are also optically thick throughout the NLR.

Note that the [O I] profile is broad, but the [S II] profile is narrow, in contrast to the general trend discussed here and in MC. As discussed further in § 5, for NGC 5548, the widths of [O I] $\lambda6300$ and [O III] $\lambda4363$, as well as the median velocity of both these lines, seem to correlate better with critical density than with ionization potential. Because NGC 5548 is unusual in other respects as well, we discuss this object in particular detail in § 6.

5. PROFILE PARAMETER CORRELATIONS

So far, the features of the profiles we have emphasized are usually obvious, and we have had little need for numerical values of profile parameters. For example, when we have noted that [O I] and [S II] profiles are narrow compared with [Fe VII], the difference in width is large enough to discern immediately by visual inspection of the profiles. Indeed, much of the discussion of line width correlations that follows is driven by the similarity of [O I] and [S II] line widths as discussed in MC. However, profile parameters are useful to confirm continuity in the sense that lines of intermediate critical density and/or ionization potential have intermediate profile parameters.

We have adopted the area-defined parameters of Whittle (1982, 1985a) with a slight modification in the wings to allow for pixels that have negative flux after continuum subtraction. In Table 2 and Figures 8–13, we present correlations involving the Whittle parameters, critical density, and ionization potential. We have chosen the median velocity, $V(50\%)$, and the interpercentile velocity width at 20%. The later is defined in Whittle (1982, 1985a) as IPV $(20\%) = a + b$, where a is the velocity (relative to the median) such that 10% of the total profile flux is blueward of a (see Fig. 7). Analogously, 10% of the total profile flux is redward of b. To be consistent with other studies, we have included analysis and discussion of emission-line blueshift. However, the sensitivity of the blueshift to details of the obscuration mechanism, which is poorly constrained, complicates the interpretation (see also Moore 1994, 1995). Therefore, we emphasize the line widths, because their correspondence to NLR kinematics is more direct than the blueshifts.

For reference, we have also included in Table 2 the value of the IPV and asymmetry functions averaged between 20% and 80% (IPV$_{avg}$ and A_{avg}), the asymmetry function at 20% ($A[20\%]$), and the kurtosis of the profiles. The asymmetry function is defined in Whittle (1982, 1985a) as

$$A(\%) = \frac{a(\%/2) - b(\%/2)}{a(\%/2) + b(\%/2)} .$$

The asymmetry function is positive for blueward extension and negative for redward extension. The kurtosis is defined in Whittle (1982, 1985a) as 2.5[IPV(50%)/IPV(10%)], where the normalization is chosen so that a Gaussian has kurtosis of 1. Kurtosis less than 1 corresponds to a profile more cusplike than a Gaussian, and the converse is true for

TABLE 2

WHITTLE PARAMETERS

| Line	$V(50\%)$ (km s^{-1})	IPV(20%) (km s^{-1})	IPV$_{avg}$ (km s^{-1})	Kurtosis	$A(20\%)$	A_{avg}
MCG 8-11-11						
Hβ λ4861.............	124	828	352	0.87	0.09	0.11
[O III] λ5007.........	92	775	340	0.90	0.07	0.06
[Fe VII] λ5721	16	646	301	1.10	0.15	0.07
He I λ5876	43	665	308	1.05	0.20	0.11
[Fe VII] λ6087	−29	867	371	0.90	0.18	0.09
[O I] λ6300	1	871	356	0.80	0.12	0.05
Hα λ6563.............	105	454	205	1.03	0.09	0.05
[S II] λ6716	78	695	299	0.91	0.08	0.03
Mrk 79						
[Fe VII] λ3760.......	−141	906	427	1.12	0.05	0.13
[Ne III] λ3869	53	440	190	0.87	0.14	0.05
Hβ λ4861.............	44	400	183	0.98	0.08	0.06
[O III] λ5007........	61	493	205	0.69	−0.05	−0.01
[Fe VII] λ6087	−30	708	295	0.90	0.30	0.15
[O I] λ6300	58	403	175	0.84	−0.04	0.00
[Fe X] λ6374........	−113	838	360	1.01	0.26	0.08
Hα λ6563.............	35	379	170	1.00	0.00	−0.01
[N II] λ6584	21	424	184	0.93	0.12	0.03
[S II] λ6731	19	313	142	1.06	0.16	0.08
Mrk 704						
[Fe VII] λ3760	−122	572	231	0.777	0.232	0.143
[Ne III] λ3869	31	449	192	0.866	0.002	−0.028
[O III] λ5007.........	62	418	183	0.911	0.061	0.015
[Fe VII] λ5721	−96	412	168	0.834	0.236	0.114
[Fe VII] λ6087	−94	649	254	0.769	0.291	0.180
[O I] λ6300	69	294	136	1.13	0.037	0.018
[Fe X] λ6374........	−102	479	215	0.96	0.093	0.040
Hα λ6563.............	−1	338	154	1.05	−0.075	−0.053
[N II] λ6584	80	305	138	1.04	0.030	0.024
[S II] λ6731	52	340	154	1.08	0.146	0.041
Mrk 841						
[O III] λ4363........	78	306	128	0.89	−0.04	−0.03
He II λ4686	70	268	114	0.92	−0.02	−0.05
Hβ λ4861.............	51	421	145	0.69	0.41	0.15
[O III] λ5007........	66	306	119	0.69	0.06	0.01
He I λ5876	53	165	73	1.02	−0.02	0.00
[Fe VII] λ6087	−138	1435	543	0.76	0.44	0.22
[O I] λ6300	39	193	84	0.94	−0.05	−0.02
[Fe X] λ6374........	−47	394	181	1.08	0.20	0.17
[N II] λ6548	48	139	62	1.02	0.13	0.06
Hα λ6563.............	39	306	117	0.72	0.12	0.04
[N II] λ6584	32	280	110	0.78	0.25	0.10
[S II] λ6716	36	186	80	0.92	0.07	0.02
[S II] λ6731	21	201	87	0.89	0.03	−0.02
NGC 4151						
[Fe VII] λ3760	−114	721	299	0.86	0.12	0.09
[Ne III] λ3869	−55	777	292	0.71	0.19	0.11
[Fe VII] λ6087	−49	791	285	0.68	0.26	0.17
[O I] λ6300	36	541	208	0.74	0.05	0.04
[Fe X] λ6374........	−156	1054	500	1.08	0.29	0.21
Hα λ6563.............	32	381	155	0.86	0.03	0.02
NGC 5548						
[Fe VII] λ3760	−376	564	252	1.03	0.05	0.04
[Ne III] λ3869	−151	574	259	0.97	0.04	0.03
[O III] λ4363........	−303	521	225	0.91	0.24	0.08
Hβ λ4861.............	−98	491	224	1.05	0.08	0.05
[O III] λ5007........	−132	547	234	0.85	0.14	0.07
[Fe VII] λ5721	−287	572	262	0.99	0.00	0.02
[Fe VII] λ6087a......	−289	717	303	0.83	0.05	0.02
[Fe VII] λ6087b......	−334	726	302	0.89	0.10	0.02
[O I] λ6300	−127	627	249	0.76	0.31	0.16
[Fe X] λ6374........	−436	762	304	0.82	0.17	0.00
Hα λ6563.............	−57	417	195	1.12	0.12	0.06
[N II] λ6584	31	283	126	1.01	0.13	0.05
[S II] λ6716	26	306	144	1.09	0.07	0.05
[S II] λ6731	19	327	149	1.04	0.07	0.02
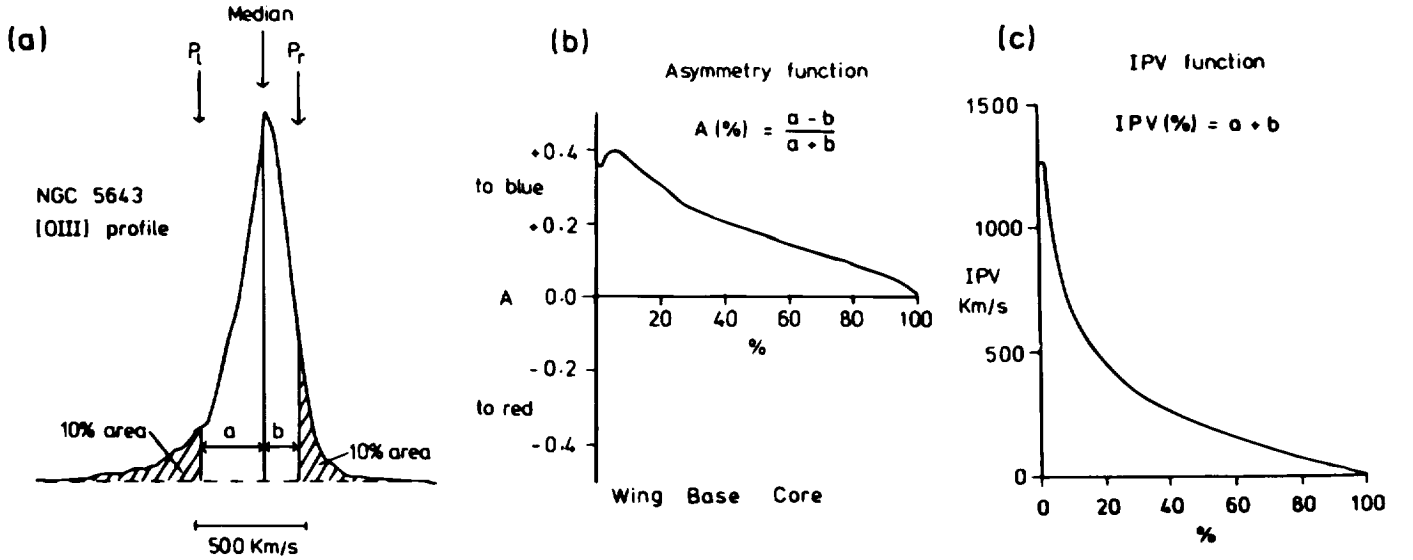
FIG. 7.—Definitions for an area parameter scheme to characterize profile asymmetry and width. (a) 10, 50, and 90 interpercentile markers in the [O III] profile of NGC 5643 (wavelength increasing to the right). Lengths a and b are used to evaluate asymmetry and width parameters A(20%) and IPV(20%), respectively. (b, c) Asymmetry and IPV functions for this profile. This figure and caption are both reproduced from Whittle (1985a). We thank Mark Whittle, as well as the MNRAS, for permission to include them here.
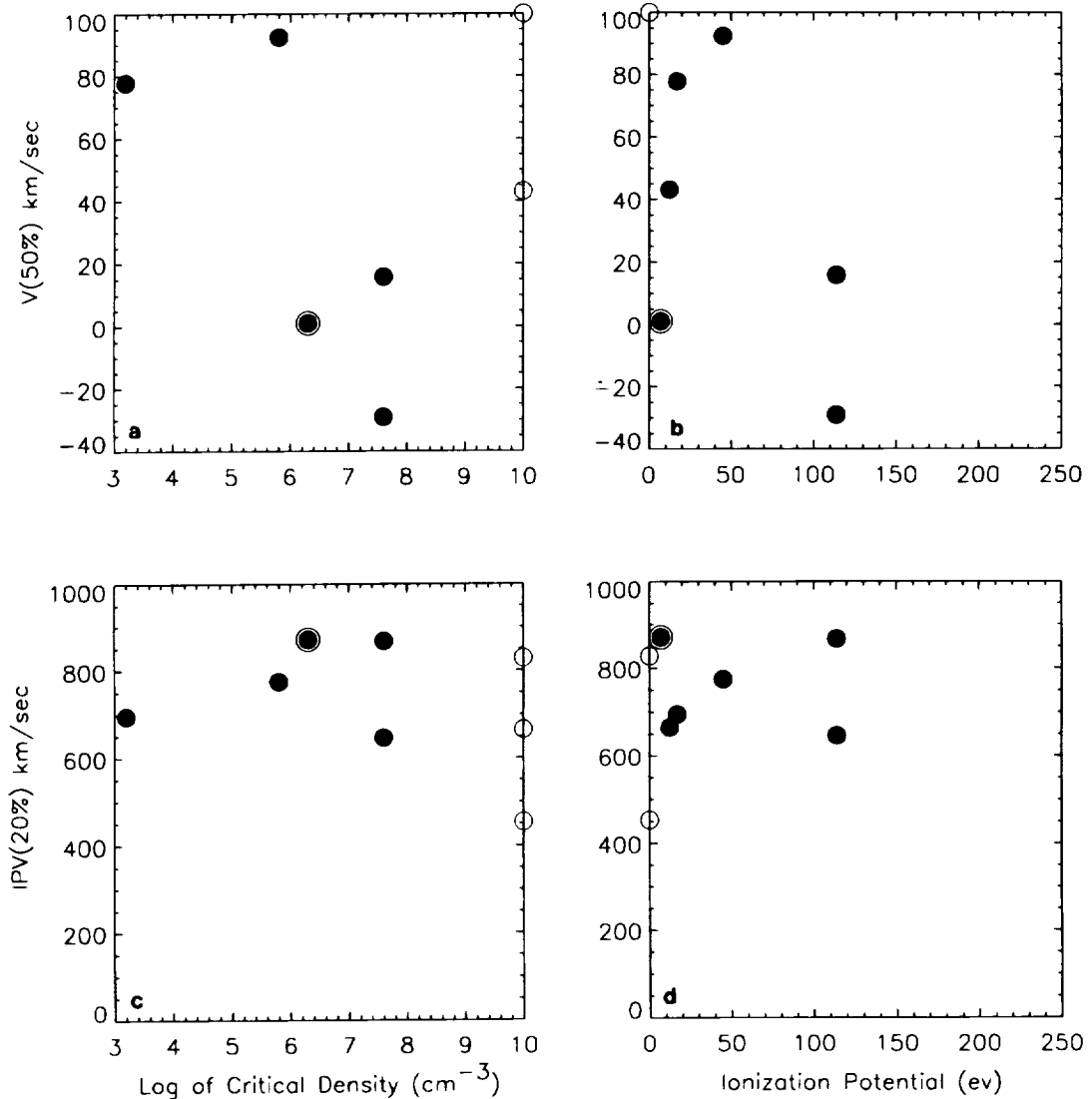

FIG. 8.—The median velocity, V(50%), and the interpercentile velocity width at 20% (see text and Fig. 7) are plotted vs. n_{cr} and IP for MCG 8-11-11. Isolated open circles represent the recombination lines, and the open circle enclosing the filled circle represents [O I] λ6300. There is no correlation of IPV(20%) with either n_{cr} or IP.
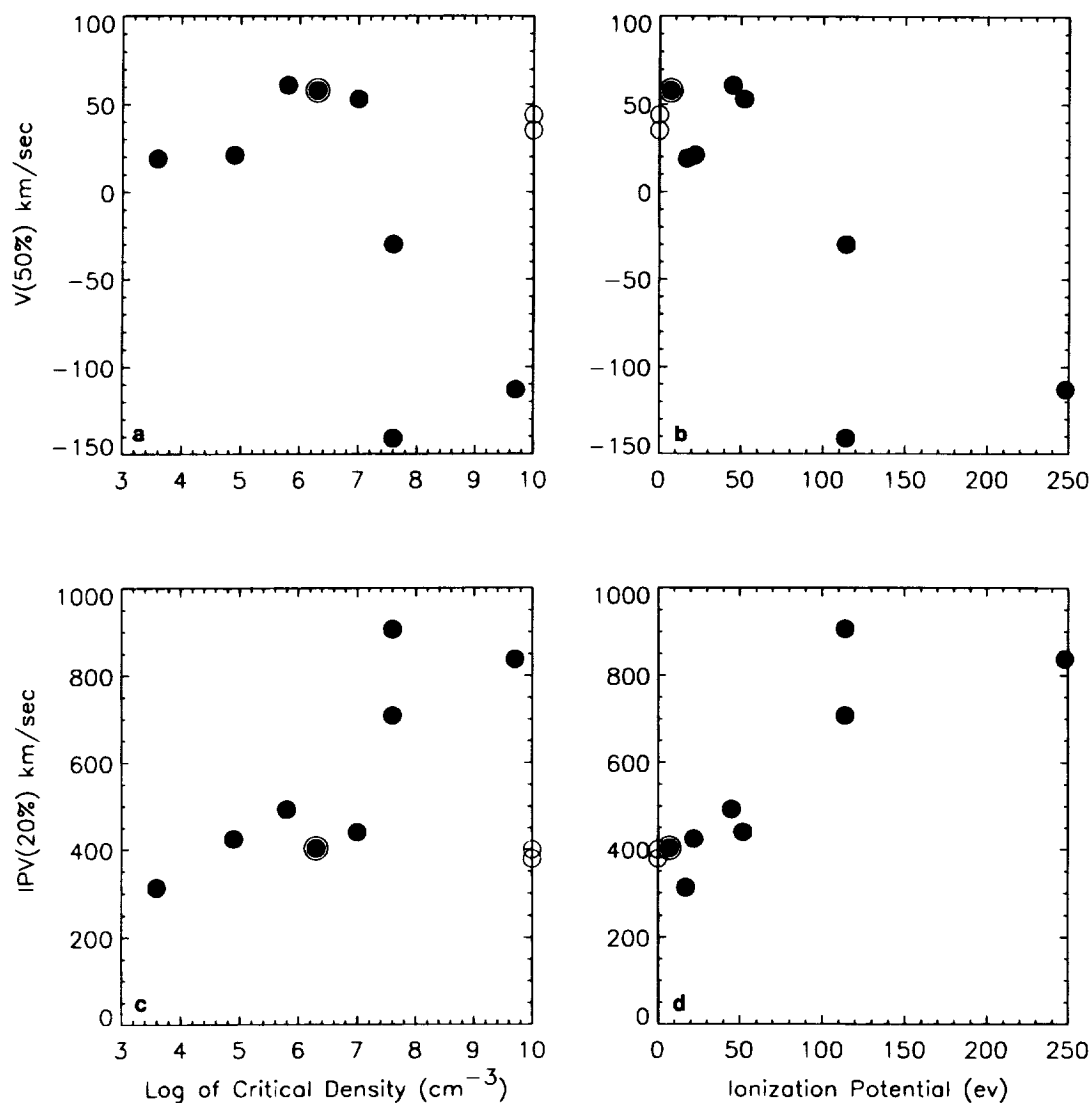
293

FIG. 9.—The median velocity, $V(50\%)$, and the interpercentile velocity width at 20% (see text) are plotted vs. n_{cr} and IP for Mrk 79. Isolated open circles represent the recombination lines. Although IPV(20%) correlates with both n_{cr} and IP, [O I] $\lambda6300$ (enclosed by an open circle) lies off the correlation on the n_{cr} plot, but it follows the correlation on the IP plot.

kurtosis greater than 1. The values of $V(50\%)$, IPV(20%), and IPV_{avg} are in units of km s^{-1}, while the kurtosis, $A(20\%)$, and A_{avg} are dimensionless.

For possible future reference, we present six additional profile parameters in Table 3. The velocity of the peak and centroid are V_{peak} and $V_{centroid}$. The remaining parameters are widths as follows. The rms velocity is $V_{rms} \equiv (\langle v^2 \rangle - \langle v \rangle^2)^{1/2}$. The full widths at $\frac{1}{4}$, $\frac{1}{3}$, and $\frac{1}{2}$ of the peak intensity are FW$\frac{1}{4}$M, FW$\frac{1}{3}$M, and FWHM, respectively. All the parameters of Table 3 are in units of km s^{-1}.

As an additional reference, we have also tabulated those emission lines we have analyzed together with their critical density and ionization potential in Table 4. As is conventional, we define the ionization potential as the arithmetic mean of the two successive stages of ionization.

In Figures 8–13, we plot $V(50\%)$ and IPV(20%) in units of km s^{-1} versus the log of n_{cr} in units cm^{-3} and versus IP in eV for all six of our objects. Because much of the discussion that follows focuses on [O I] $\lambda6300$ and [O III] $\lambda4363$ as the lines that can potentially discriminate between correlations with n_{cr} and correlations with IP, we highlight

the data points corresponding to these lines by enclosing them with open circles. The isolated open circles represent Hα and Hβ. Although the critical density and ionization potential are not physically meaningful for the recombination lines, the profiles contain information. In stratified clouds, the recombination lines are emitted most efficiently in a zone of intermediate ionization, in which [O III] and [Ne III] are also emitted. Due to the relatively large uncertainties of subtracting the underlying broad component from the narrow component, it is not appropriate here to attach much significance to the similar velocity shifts (and line widths) of the Balmer lines and the lines of [O III] $\lambda5007$ and [Ne III] $\lambda3869$. However, we suggest that the recombination lines should be included in similar analyses of Seyfert 2 galaxies.

For NGC 5548, correlations of both $V(50\%)$ and IPV(20%) are clearly with n_{cr} rather than with IP, making this object a counterexample to the general trend discussed here and in MC. Therefore, we discuss the correlations for NGC 5548 separately. For the other objects, correlations are less clear, particularly the correlation with $V(50\%)$.
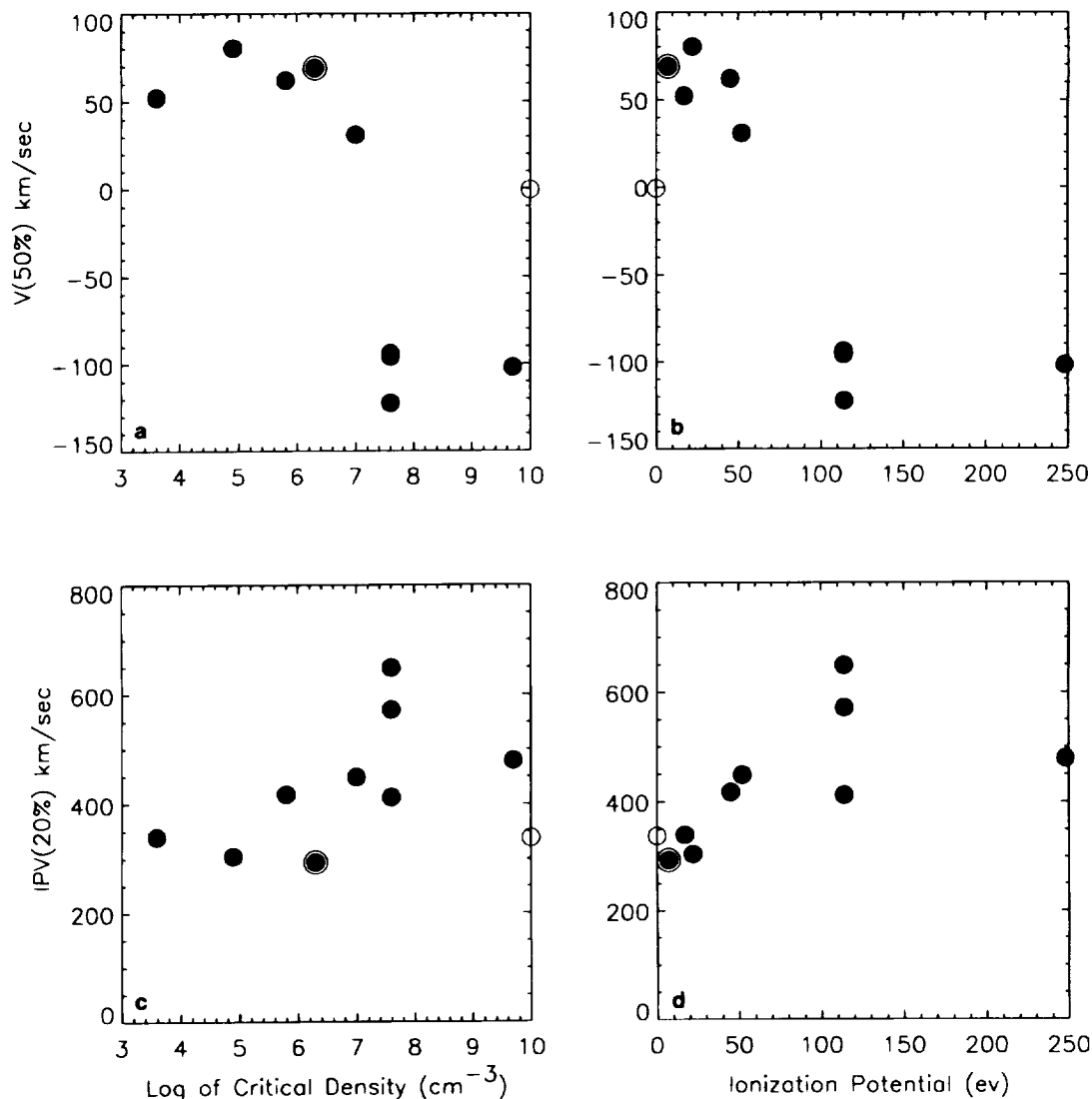
Fig. 10.—The median velocity, $V(50\%)$, and the interpercentile velocity width at 20% (see text) are plotted vs. n_{cr} and IP for Mrk 704. Isolated open circles represent the recombination lines. Although IPV(20%) correlates with both n_{cr} and IP, [O I] $\lambda6300$ (enclosed by an open circle) lies off the correlation on the n_{cr} plot but follows the correlation on the IP plot.

Ultimately, possible correlations between $V(50\%)$ and/or IPV(20%) with n_{cr} and/or IP must be accepted or rejected by comparing visually the scatter in the result with some systematic trend or lack thereof. Error bars that truly reflect a quantitative uncertainty in the parameters in cases in which nonformal errors dominate, such as that of [Fe x] $\lambda6374$, are virtually impossible to estimate reliably. Only in the case in which the adjacent continuum is nearly flat or linear, and featureless, and in which there are no blends with other lines, are the true uncertainties approximated reasonably well by formal error estimates.

We estimated formal errors by choosing the [O III] $\lambda5007$ profile in NGC 5548 as a fiducial model profile. We added a linear continuum and noise to the profile, subtracted a linear fit to the continuum, and calculated $V(50\%)$ and IPV(20%) for the resulting profile. We repeated the procedure 10 times and calculated the standard deviation in the 10 calculated values of $V(50\%)$ and IPV(20%). We repeated the experiment with varying amounts of noise and continuum strength and slope. For fixed S/N in the final continuum-subtracted profile, the standard deviations are

not very sensitive to either the strength or the slope of the synthetic continuum. The reason is that we know a priori the functional form of the adjacent continuum, though this, of course, is not the case for the real data. The standard deviations are also not very sensitive to the precise choice of profile limits, though this again is at least partly an artifact of the continuum subtraction being more reliable than it is for the real data.

Letting f be the noise added to the profile relative to the peak of the profile, the standard deviation in $V(50\%)$ increases linearly from 0 to 70 km s^{-1} as f is increased from 0 to 0.3. For IPV(20%), the standard deviation increases linearly from 0 to 230 km s^{-1}. (The standard deviation curves are more complicated for $f \gtrsim 0.3$.) The noisiest profiles that we analyzed have $f \lesssim 0.1$. It follows that the scatter in the following plots that do not show correlations (as well as those that do) is due mostly to either nonformal errors or to the likelihood that the objects are more complicated than justifies assuming an intrinsic one-to-one correspondence between line width and n_{cr} and/or IP. In Paper II, for example, we present synthetic correlations resulting from
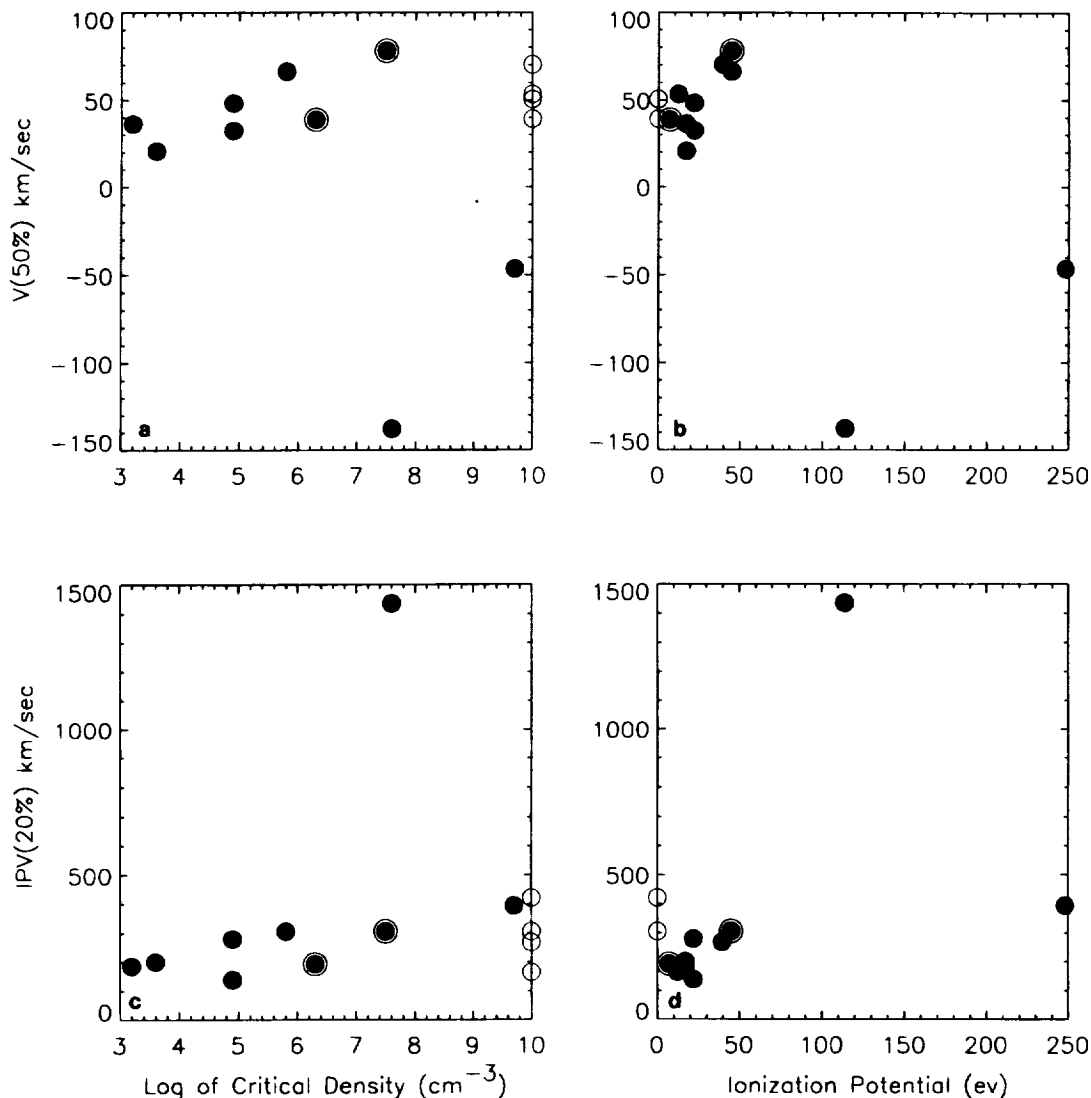
FIG. 11.—The median velocity, $V(50\%)$, and the interpercentile velocity width at 20% (see text) are plotted vs. n_{cr} and IP for Mrk 841. Isolated open circles represent the recombination lines, and open circles enclosing the filled circles represent [O I] $\lambda6300$ and [O III] $\lambda4363$. It is inconclusive whether correlations are with IP or n_{cr} because only the [Fe] lines, which have both high n_{cr} and high IP, stand out.

models, in which scatter comparable to that observed is intrinsic to the model.

Now we present and discuss the correlations for individual objects. For each correlation, we also calculate a linear correlation coefficient, R, together with the corresponding probability of chance occurance, P_{null}.

MCG 8-11-11 (Fig. 8).—$V(50\%)$ appears to correlate better with n_{cr} than with IP. However, because [O III] $\lambda5007$ is not blueshifted relative to [S II] $\lambda6716$, any correlation between blueshift and critical density that might be inferred from Figure 8a is at best tenuous. There is no correlation of IPV(20%) with either n_{cr} or IP (we have already noted in § 5.1 that the widths, as well as the profiles, of lines of both high and low IP are similar in this object). For MCG 8-11-11, R/P_{null} are $-0.73/0.16$ for $V(50\%)$ versus n_{cr}, $-0.50/0.39$ for $V(50\%)$ versus IP, $0.27/0.66$ for IPV(20%) versus n_{cr}, and $-0.18/0.78$ for IPV(20%) versus IP, respectively.

Mrk 79 (Fig. 9).—It appears that the highest critical density lines are blueshifted relative to the low critical density lines (Fig. 9a). Note, however, that these lines have high IP and that [O I] $\lambda6300$ is associated with the lines of

low-ionization potential rather than with those of high critical density. Although a correlation with n_{cr} is apparent visually, to interpret Figure 9a as a correlation of $V(50\%)$ with n_{cr}, we must suppose that $V(50\%)$ is roughly constant over four decades in critical density and then changes rapidly over an additional factor of order unity in n_{cr}. For IPV(20%), $\lambda6300$ lies off the correlation on the critical density plot (Fig. 9c) but follows the correlation on the ionization potential plot (Fig. 9d). The values of R/P_{null} are $-0.64/0.08$ for $V(50\%)$ versus n_{cr}, $-0.79/0.02$ for $V(50\%)$ versus IP, $0.83/0.02$ for IPV(20%) versus n_{cr}, and $0.84/0.01$ for IPV(20%) versus IP, respectively.

Mrk 704 (Fig. 10).—On the $V(50\%)$ correlation, the [O I] line fits on both the n_{cr} and the IP relations. On the IPV plot, the [O I] line fits well on the IP correlation and falls out of place on the n_{cr} correlation. The values of R/P_{null} are $-0.79/0.01$, $0.61/0.08$, $-0.82/0.006$, and $0.58/0.10$.

Mrk 841 (Fig. 11).—For all the correlations for Mrk 841, only the [Fe VII] and [Fe X] lines stand out. It is inconclusive whether correlations are with IP or with n_{cr} because these lines have both high IP and high n_{cr}. The values of R/P_{null} are $-0.46/0.22$, $-0.62/0.07$, $0.44/0.24$, and $0.40/0.28$.

TABLE 3
Additional Profile Parameters

Line	V_{peak}	V_{centroid}	V_{rms}	FW$\frac{1}{4}$M	FW$\frac{1}{3}$M	FWHM
MCG 8-11-11						
[O ɪɪ] λ3727......	71	−46	395	1134	1011	823
Hβ λ4861	115	48	331	888	764	544
[O ɪɪɪ] λ5007	119	19	323	899	757	624
[Fe vɪɪ] λ5721......	126	−50	279	895	811	607
He ɪ λ5876.........	83	−26	288	810	748	650
[Fe vɪɪ] λ6087......	136	−106	351	955	846	606
[O ɪ] λ6300........	117	−74	390	912	755	577
Hα λ6563	121	56	197	611	544	413
[S ɪɪ] λ6716........	64	30	287	1185	690	555
Mrk 79						
[O ɪɪ] λ3727........	23	−46	201	725	658	550
[Fe vɪɪ] λ3760......	−160	−249	318	1009	1003	854
[Ne ɪɪɪ] λ3869	−12	−49	179	528	464	433
Hβ λ4861	18	−30	159	509	451	367
[O ɪɪɪ] λ5007	−7	25	260	506	452	425
[Fe vɪɪ] λ6087......	−4	−119	316	733	593	415
[O ɪ] λ6300........	25	53	241	456	400	353
[Fe x] λ6374	−31	−201	306	906	772	570
Hα λ6563	−8	3	171	458	422	342
[N ɪɪ] λ6584........	−16	−27	195	471	425	344
[S ɪɪ] λ6731.........	13	−32	132	409	383	313
Mrk 704						
[O ɪɪ] λ3727........	92	43	179	737	597	448
[Fe vɪɪ] λ3760......	−175	−257	190	627	402	298
[Ne ɪɪɪ] λ3869	−70	−50	183	512	446	362
[O ɪɪɪ] λ5007	0	−12	161	476	429	393
[Fe vɪɪ] λ5721......	−103	−158	185	483	315	233
[Fe vɪɪ] λ6087......	−94	−181	303	511	410	262
[O ɪ] λ6300........	42	30	256	416	379	315
[Fe x] λ6374	−116	−155	217	544	576	460
Hα λ6563	−67	−29	148	457	401	318
[N ɪɪ] λ6584........	60	42	135	405	365	292
[S ɪɪ] λ6731.........	104	26	137	473	439	305
Mrk 841						
[O ɪɪ] λ3727........	−55	31	203	552	515	445
[O ɪɪɪ] λ4363	−3	7	112	394	347	218
He ɪɪ λ4686	−12	13	102	351	280	206
Hβ λ4861	4	−53	155	300	283	212
[O ɪɪɪ] λ5007	0	−2	153	296	258	189
He ɪ λ5876..........	14	20	71	246	197	148
[Fe vɪɪ] λ6087......	3	−351	588	1337	718	639
[O ɪ] λ6300........	0	6	90	233	204	166
[Fe x] λ6374	−58	−112	160	491	438	313
[N ɪɪ] λ6548........	21	12	61	197	169	128
Hα λ6563	9	−5	148	267	231	171
[N ɪɪ] λ6584........	10	−20	127	258	216	164
[S ɪɪ] λ6716.........	4	−2	87	224	192	150
[S ɪɪ] λ6731.........	1	4	89	224	203	167
NGC 4151						
[O ɪɪ] λ3727........	−137	−116	301	795	723	543
[Fe vɪɪ] λ3760......	−105	−217	280	988	907	678
[Ne ɪɪɪ] λ3869	−107	−107	320	644	511	370
[Fe vɪɪ] λ6087......	−2	−89	372	520	390	283
[O ɪ] λ6300.........	4	−33	231	500	391	245
Fe x λ6374	−2	−233	437	1092	995	543
Hα λ6563	−1	−7	166	443	353	240
NGC 548						
[Fe vɪɪ] λ3760......	−430	−430	224	1478	1141	490
[Ne ɪɪɪ] λ3869	−149	−243	236	682	610	507
[O ɪɪɪ] λ4363	−325	−387	224	677	573	470
Hβ λ4861	−129	−174	182	621	588	484
[O ɪɪɪ] λ5007	−164	−227	248	605	538	411
[Fe vɪɪ] λ6087......	−325	−323	324	790	675	545
[O ɪ] λ6300........	−120	−219	275	542	464	329
[Fe x] λ6374	−556	−494	301	777	633	500
Hα λ6563	−65	−105	179	560	517	424
[N ɪɪ] λ6584........	33	−12	121	378	323	243
[S ɪɪ] λ6716.........	17	−11	127	407	366	300
[S ɪɪ] λ6731.........	−19	−21	131	422	393	307

TABLE 4

EMISSION LINES, λ, n_{cr}, AND IP

Wavelength (Å)	Ion	n_{cr} (cm^{-3})	Mean Ionization Potential (eV)
3726.1	[O II]	3.2×10^3	24
3728.8	[O II]	6.3×10^2	24
3760.3	[Fe VII]	4.0×10^7	114
3868.8	[Ne III]	1.0×10^7	52
4363.2	[O III]	3.2×10^7	45
4685.7	He II	...	40
4861.3	H I	...	...
5006.8	[O III]	6.3×10^5	45
5721.1	[Fe VII]	4.0×10^7	114
5875.7	He I	...	12
6086.9	[Fe VII]	4.0×10^7	114
6300.3	[O I]	2.0×10^6	7
6374.6	[Fe X]	5.0×10^9	248
6548.1	[N II]	7.9×10^4	22
6562.8	H I	...	...
6583.4	[N II]	7.9×10^4	22
6716.4	[S II]	1.6×10^3	17
6730.8	[S II]	4.0×10^3	17

NGC 4151 (Fig. 12).—Because we do not have [S II] $\lambda6716, 6731$ profiles from NGC 4151 (and [O II] $\lambda3727$ is an unresolved blend), all we can say about this object, based on our data alone, is that the highest IP/n_{cr} lines are blueshifted and broad relative to [O I] $\lambda6300$. However, if we were to include the [S II] profiles of Veilleux (1991a), we would put NGC 4151 in the same category as MCG 8-11-11 (no correlation of IPV with either ionization potential or critical density).

NGC 5548 (Fig. 13).—Because the [O I] profile in NGC 5548 is broad and that of [S II] is narrow, NGC 5548 stands in striking contrast to the general trend discussed here and in MC. In Figures 13a and 13b, we plot the median velocity (V[50%]) of the emission lines from NGC 5548 versus both the critical density and the ionization potential, respectively. The velocities are relative to a 21 cm measurement of the systemic velocity.

As stated already, for NGC 5548, correlations of both V(50%) and IPV(20%) are clearly with n_{cr} rather than with IP. There is a good correlation between blueshift and criti-
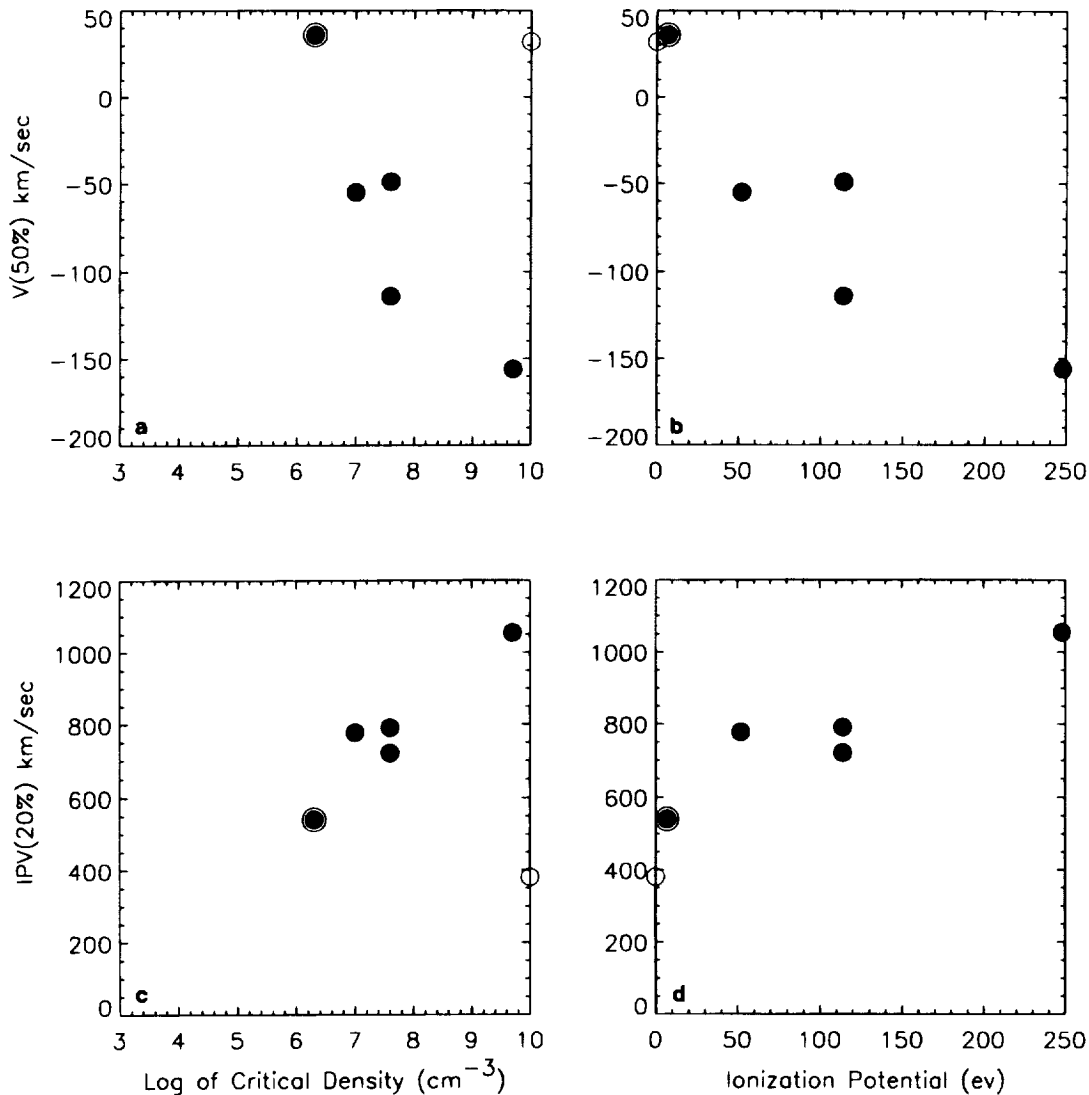

FIG. 12.—The median velocity, V(50%), and the interpercentile velocity width at 20% (see text) are plotted vs. n_{cr} and IP for NGC 4151. Isolated open circle represents Hα, and open circle enclosing the filled circle represents [O I] $\lambda6300$. If we were to include the [S II] $\lambda\lambda6716, 6731$ lines of Veilleux (1991a), we would infer no correlation of IPV(20%) with either n_{cr} or IP.
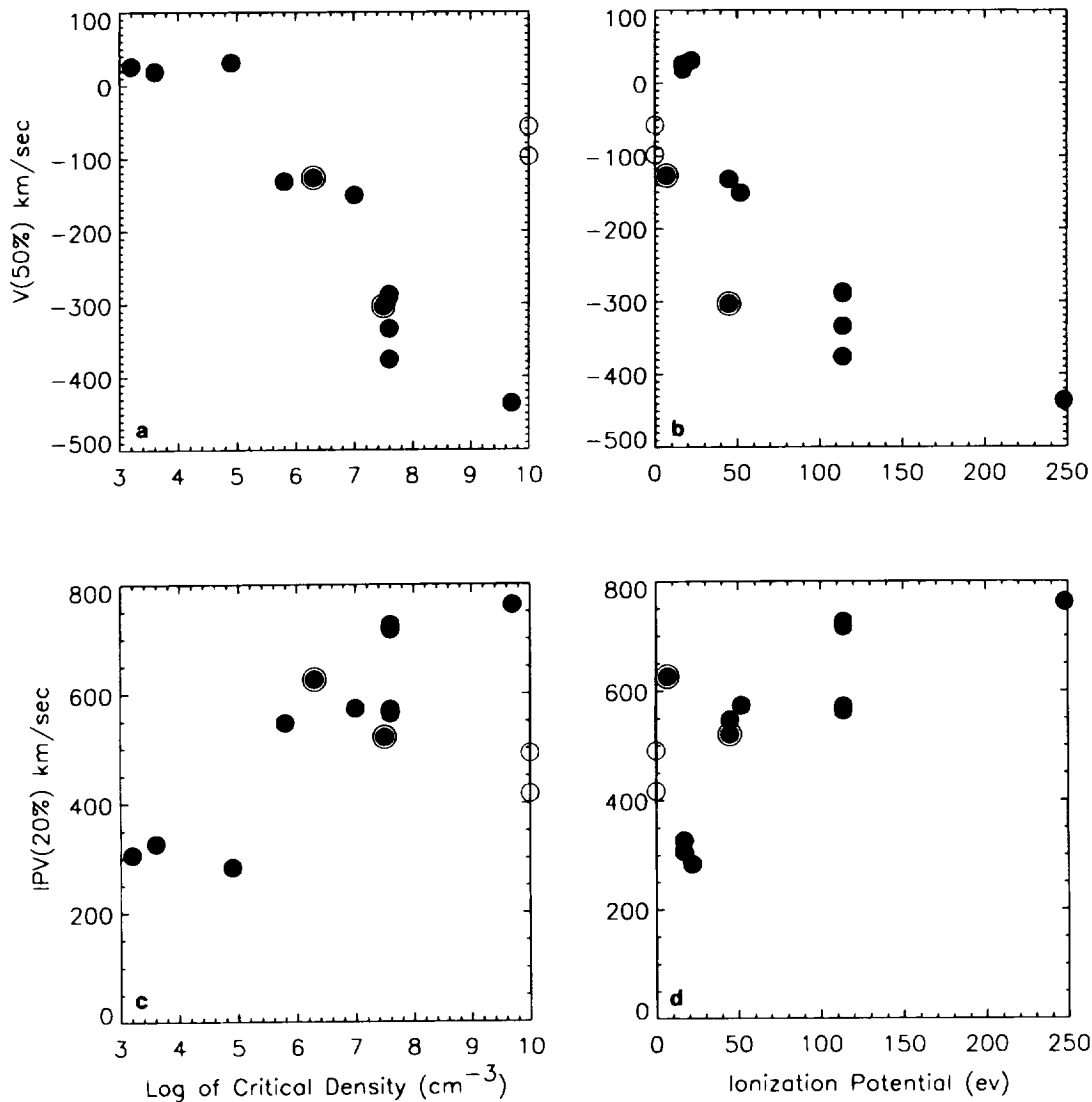
Fig. 13.—The median velocity, $V(50\%)$, and the interpercentile velocity width at 20% (see text) are plotted vs. n_{cr} and IP for NGC 5548. Isolated open circles represent the recombination lines. The important [O I] $\lambda6300$ and [O III] $\lambda4363$ data points are enclosed by open circles. Correlations of both $V(50\%)$ and IPV(20%) are clearly with n_{cr} rather than with IP. This is in contrast to the general trend discussed here and in MC.

cal density in NGC 5548. Although there is apparently a good correlation between blueshift and ionization potential as well, there are two points on the $V(50\%)$ versus ionization potential plot that deviate. That these deviant points represent [O I] $\lambda6300$ and [O III] $\lambda4363$ is not surprising because, of the lines commonly analyzed in the literature, it is these two that deviate from a correlation of critical density with ionization potential.

Note that the velocity shift from systemic is very large (≈ 400 km s^{-1}) for the forbidden Fe lines in NGC 5548. The shift is large enough that one may suspect an error in the wavelength calibration. This is not the case, however, because the wavelength calibration matches the known wavelengths of the night-sky lines to a precision of 25 km s^{-1}. One might also speculate that the 21 cm systemic velocity measurement is not representative of the NLR center-of mass velocity. However, the 21 cm systemic velocity agrees (within 40 km s^{-1}) with $V(50\%)$ of the lowest critical density lines. Regardless of the systemic velocity, the Fe lines are blueshifted by about 400 km s^{-1} relative to the

lowest critical density lines. Thus, NGC 5548 is also unusual in its large blueshift in $V(50\%)$ of the Fe lines.

In Figures 13c and 13d, we plot IPV (20%) versus, n_{cr} and IP. Again, [O I] $\lambda6300$ deviates from the otherwise well-defined correlation on the IP plot but does not deviate on the n_{cr} plot. The above correlations for NGC 5548 are consistent with velocity decreasing outward because lines of high critical density are systematically broader than lines of low critical density. In our previous discussion, we have assumed that all Seyfert NLRs are fundamentally similar and can be described by models differing only in, e.g., N_{col}/N_{min} at v_{min}. Although the line profiles (especially that of [Fe X] $\lambda6374$) are similar to the profiles of the other objects in our sample, the correlations suggest an NLR with fundamentally different kinematics. In MC, we suggested that at 5 Å and 10 Å resolution, $\lambda4363$ line widths may have been systematically overestimated in Seyfert 1 galaxies because of difficulties in deblending from the broad and narrow components of Hγ. Even with our higher resolution, we may be subject to the same effect as well. However, the

dilemma in which line widths of NGC 5548 seem to correlate fundamentally with critical density rather than with ionization parameter is posed by *both* $\lambda 4363$ and $\lambda 6300$. The (highly significant) values of R/P_{null} are $-0.94/5.0 \times 10^{-6}$, $-0.83/9.2 \times 10^{-4}$, $0.88/1.8 \times 10^{-4}$, and $0.71/9.7 \times 10^{-3}$.

6. SUMMARY

The most important observational feature of the profiles presented here is that for lines encompassing a wide range of critical density and ionization potential, the variation of flux with projected velocity is very similar in some objects (e.g., MCG 8-11-11 and NGC 4151). This is inconsistent with a scenario in which lines of low and high critical density and/or ionization potential are formed in physically distinct regions. Thus, we expect comparable spatial extents for emission into each line. We have proposed testing this hypothesis with coordinated *Hubble Space Telescope* and ground-based spectrophotometry of the applicable NLRs that can be spatially resolved on an angular scale ($\lesssim 2''$) that properly complements analyses of existing spatially integrated emission-line spectra. In some other objects, lines of high critical density and/or ionization potential are systematically broader than those of low critical density and/or ionization potential (e.g., Mrk 79, Mrk 704, and Mrk 841). It is possible to explain the difference between the two types of objects in terms of a relatively small difference in the cloud column density throughout the NLR (see Paper II, MC, and Moore [1994]). If clouds at small r have $N_{col} \approx 10^{24}$ cm^{-2}, then even with $N_{col} \propto r^{-4/3}$ (constant mass spherical clouds with $n_e \propto r^{-2}$), it is possible to have $N_{col} > N_{min}$ ($\approx 10^{22}$ cm^{-2} for $\Gamma = 0.3$) throughout the NLR so that each cloud emits both [O I] and [Fe VII]. If clouds start out with N_{col} less by a modest factor, then N_{col} falls to less than N_{min} before clouds reach their maximum velocity at large r, and an [O I] profile narrower than that of [Fe VII] results.

Overall, our sample of Seyfert 1 galaxies confirms the well-known correlations of line width and blueshift with ionization potential and/or critical density. A sample the size of ours cannot alone confirm or refute properly the conclusion of MC that the correlations are fundamentally with ionization potential rather than with critical density, especially given that our sample includes one unusual counter example (NGC 5548). The correlations for Mrk 841 are not conclusive because the only lines that stand out are [Fe VII] $\lambda 6087$ and [Fe X] $\lambda 6374$, which have both high critical density and high ionization potential. This leaves just four objects, MCG 8-11-11, Mrk 79, Mrk 704, and NGC 4151, to support our earlier conclusion (correlations with ionization potential). Nevertheless, these four objects do follow the trend discussed in MC; the objects with broad [O I] profiles (MCG 8-11-11 and NGC 4151) also have broad [S II] profiles, and the objects with narrow [O I] profiles (Mrk 79 and Mrk 704) have narrow [S II] profiles.

REFERENCES

Appenzeller, I., & Östreicher, R. 1988, AJ, 95, 45
Boksenberg, A., Shortridge, K., Allen, D. A., Fosbury, R. A. E., Penston, M. V., & Savage, A. 1975, MNRAS, 173, 381
Capriotti, E., Foltz, C., & Byard, P. 1981, ApJ, 245, 396
Cohen, R. D. 1983, ApJ, 273, 489
Dahari, O., & De Robertis, M. M. 1988, ApJS, 67, 249
De Robertis, M. M., & Osterbrock, D. E. 1984, ApJ, 286, 171
———. 1986, ApJ, 301, 727
De Robertis, M. M., & Shaw, R. A. 1990, ApJ, 348, 421
Heckman, T. M., Balick, B., & Sullivan, W. T. III. 1978, ApJ, 224, 745
Heckman, T. M., Miley, G. K., van Breugel, W. J. M., & Butcher, H. R. 1981, ApJ, 247, 403
Komossa, S., & Schulz, H. 1994, in STSci Symp. Ser., 8 The Analysis of Emission Lines, ed. R. E. Williams & M. Livio (Baltimore: STScI), 30
Krinsky, I. S., & Puetter, R. C. 1992, ApJ, 394, 472
Moore, D. 1994, Ph.D. thesis Univ. California, San Diego
———. 1995, in preparation

Moore, D., & Cohen, R. D. 1994, ApJ, 433, 602 (MC)
———. 1996, ApJ, 470, 301 (Paper II)
Oke, J. B., & Gunn, J. E. 1982, PASP, 94, 586
Osterbrock, D. E. 1981, ApJ, 246, 696
Penston, M. V., Fosbury, R. A. E., Boksenberg, A., Ward, M. J., & Wilson, A. S. 1984, MNRAS, 208, 347
Tsvetanov, Z. I., Kriss, G. A., Evans, I. N., & Ford, H. C. 1994, BAAS, 26, 966
Veilleux, S. 1988, AJ, 95, 1695
———. 1991a, ApJS, 75, 357
———. 1991b, ApJ, 369, 331
Whittle, M. 1982, Ph.D. thesis, Cambridge Univ.
———. 1985a, MNRAS, 213, 1
———. 1985b, MNRAS, 216, 817
———. 1991, in Testing the AGN Paradigm, ed. S. S. Holt, S. G. Neff, & M. C. Urry (New York: AIP), 607